THE MILLENNIUM ARECIBO 21-CM ABSORPTION LINE SURVEY. II. PROPERTIES OF THE WARM AND COLD NEUTRAL MEDIA

Carl Heiles

Astronomy Department, University of California, Berkeley, CA 94720-3411; cheiles@astron.berkeley.edu

T.H. Troland

Department of Physics and Astronomy, University of Kentucky, Lexington, KY 40506; troland@pa.uky.edu

ABSTRACT

We use the Gaussian-fit results of Paper I to investigate the properties of interstellar HI in the Solar neighborhood. The Warm and Cold Neutral Media (WNM and CNM) are physically distinct components. The CNM spin temperature histogram peaks at about 40 K.

About 60% of all HI is WNM; there is no discernable change in this fraction at $z = 0$. At $z = 0$, we derive a volume filling fraction of about 0.50 for the WNM; this value is very rough. The upper-limit WNM temperatures determined from line width range upward from $\sim$ 500 K; a minimum of about 48% of the WNM lies in the thermally unstable region 500 to 5000 K. The WNM is a prominent constituent of the interstellar medium and its properties depend on many factors, requiring global models that include all relevant energy sources, of which there are many.

We use Principal Components Analysis, together with a form of least squares fitting that accounts for errors in both the independent and dependent parameters, to discuss the relationships among the four CNM Gaussian parameters. The spin temperature T_s and column density $N(HI)$ are, approximately, the two most important eigenvectors; as such, they are sufficient, convenient, and physically meaningful primary parameters for describing CNM clouds. The Mach number of internal macroscopic motions for CNM clouds is typically 2.5, but there are wide variations. We discuss the historical τ_0-T_s relationship in some detail and show that it has little physical meaning.

We discuss CNM morphology using the CNM pressure known from UV stellar absorption lines. Knowing the pressure allows us to show that CNM structures cannot be isotropic but instead are sheetlike, with length-to-thickness aspect ratios ranging up to about 280. We present large-scale maps of two regions where CNM lies in very large "blobby sheets".

We test the McKee/Ostriker model of the interstellar medium by explicitly modeling our data with CNM cores contained in WNM envelopes. This modeling scheme works quite well for many sources but has several serious deficiencies.

Contents

1. INTRODUCTION

This paper discusses the astronomically oriented results of a new Arecibo[1] 21-cm absorption line survey; it is the comprehensive version of the preliminary report by Heiles (2001b). Paper I (Heiles and Troland 2002) discusses the observational and data reduction techniques.

We took great care in accounting for instrumental gain fluctuations and angular structure of HI so that we could derive accurate opacity and expected emission profiles, including realistic uncertainties. (An expected profile is the emission profile towards the source that would be observed if the source flux were zero). The opacity profiles come from the Cold Neutral Medium (CNM) and are characterized by distinct peaks; we decomposed them into Gaussian components. The expected profiles are produced by both the Warm Neutral Medium (WNM) and the CNM. We fit them using a simple but physically correct radiative transfer equation that includes both the emission and absorption of the CNM and, in addition, one or a few independent Gaussians for the WNM emission. We discussed the fitting process and its uncertainties in detail, and presented many examples of the technique. We derived spin temperatures for the CNM using the opacity and expected profiles. We derived upper-limit temperatures for the CNM using the line widths. We presented all results in tabular, graphical, and electronic form.

Table 1 summarizes the sources observed and the column densities of CNM and WNM. Here, by "WNM", we mean Gaussian components detected only in emission, and by "CNM" we mean Gaussians that were detected in absorption. Paper I presents the full table of Gaussian component properties. We have a total of 79 sources, 202 CNM components, and 172 WNM components. 13 sources have $|b| < 10^\circ$, and we exclude these from some of our discussion below because their profiles are complicated or the WNM linewidths might be significantly broadened by Galactic rotation.

§2.1 shows that the division between WNM and CNM is not only observational, but also physical; §2.3.2 summarizes the statistics on CNM/WNM column densities for the Gaussians. §3 presents column density statistics for the lines of sight for the CNM and WNM. §4 discusses the volume filling fraction of the WNM, both at high and low z.

The next few sections discuss the basic statistical properties of the Gaussian components. §5 presents statistics on V_{LSR}. §6 presents correlations among the four parameters that describe the CNM components. The reader interested in these correlations should consult the two subsequent sections: §7 shows that inadequate angular resolution might affect these correlations, and §8 shows that CNM features are sheetlike and not isotropic with the consequence that angular resolution effects are far less important than found in §7.

§9 re-reduces all the data of Paper I in terms of the McKee & Ostriker (1977) (MO) model, with each CNM component surrounded by an independent WNM component; it is gratifyingly

[1]The Arecibo Observatory is part of the National Astronomy and Ionosphere Center, which is operated by Cornell University under a cooperative agreement with the National Science Foundation.

successful for most sources but some MO predictions are not quantitatively fulfilled. §10 presents two descriptive models; the second, the clumpy sheet model for the CNM, applies to our data.

§11 is a summary, and §12 is a commentary on the importance of the WNM for understanding not only the ISM but also its multiplicity of energy sources and the Universe at large.

2. THE CNM: AN OBSERVATIONALLY AND PHYSICALLY DISTINCT TEMPERATURE COMPONENT

2.1. Distribution of CNM and WNM spin and kinetic temperatures for $|b| > 10^\circ$

At $|b| > 10^\circ$, for the WNM we have 143 components from 66 lines of sight, each of which is a radio source, containing a total $N(HI)_{WNM,20} = 292$ and for the CNM we have a total of 143 components from 48 sources containing a total $N(HI)_{CNM,20} = 188$; the subscript 20 on $N(HI)$ means that the units are 10^{20} cm^{-2}. There are fewer CNM sources because 18 sources had undetectable absorption.

For the CNM we have direct, fairly accurate measurements of T_s derived from the fitting process described in Paper I (§4.3). For the CNM, the spin temperature is equal to the kinetic temperature. For the WNM we have rough *lower* limits on T_s from the absence of WNM absorption in the opacity profiles. For both the CNM and WNM, we have *upper* limits on kinetic temperature T_{kmax} from the line width. For warm, low-density gas T_s is not necessarily equal to the kinetic temperature, with $T_s < T_k$; for equilibrium conditions, this inequality becomes serious only for $T_k \gtrsim 1000$ K (Liszt 2001). Thus, our lower limit on T_s is also a lower limit on T_K, so T_K is bracketed; and for $T_s \lesssim 1000$ K, $T_s \approx T_k$.

Figure 1 compares either T_s (CNM components) or lower limits on T_s (WNM components) with T_{kmax} for every Gaussian component at $|b| > 10^\circ$. For the CNM components we show errorbars for T_s; for the WNM component T_s is a lower limit, so its errorbars go in only one direction and are arbitrarily set to be half the estimated value. Because $T_s \leq T_k$ and $T_{kmax} \geq T_k$, the points should all fall below the diagonal line. Nearly all of them do. There are five serious exceptions for which the difference is significantly larger than the error: a CNM component in each of 3C123, 3C237, and 4C32.44; and a WNM component in each of 3C93.1 and NRAO140. The profiles of all these sources are complicated, increasing the chance that the choice of Gaussians is not realistic. Thus there is general agreement with the requirement that all points fall below the line. In fact, most points fall well below the line, particularly for the CNM.

Figure 2 displays the temperature distributions of the WNM and the CNM. The upper two plots are for the WNM where we plot both the number of Gaussian components $N_{G,WNM}$, and the column density of these Gaussians $N(HI)_{WNM,20}$, versus T_{kmax}. The two lower plots show the analogous temperature distributions for the CNM, plotted versus T_s. In all cases, solid and dotted lines are for $|b| < 10^\circ$ and $|b| < 10^\circ$, respectively. We separate the Galactic plane sources

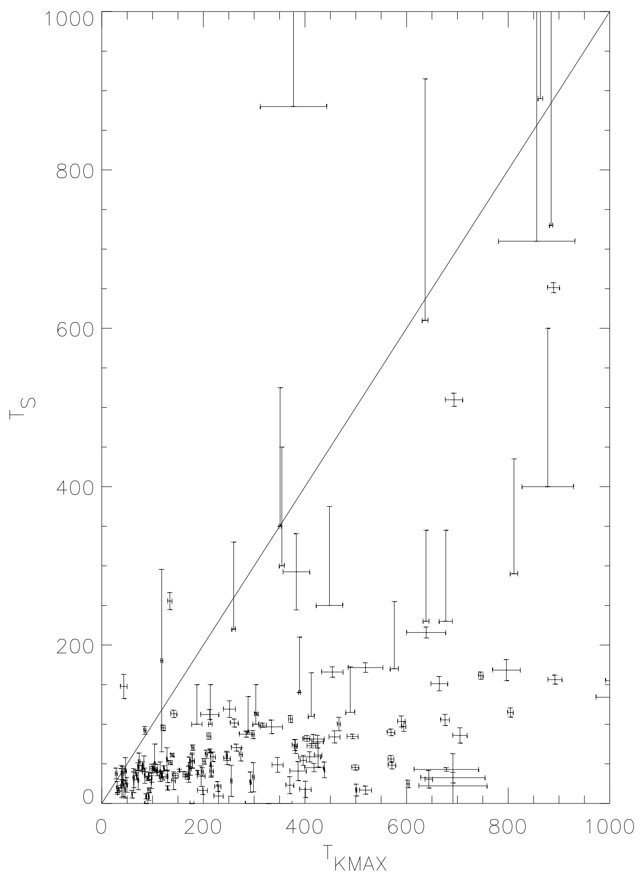

Fig. 1.— Spin temperature T_s versus upper-limit kinetic temperature T_{kmax} for all Gaussian components, both CNM and WNM, for sources having $|b| > 10°$. WNM errorbars only go up because they are lower limits.

having $|b| < 10°$ for three reasons: (1) their profiles have high column densities and dominate the $N(HI)_{20}$ histograms; (2) their profiles are broadened by Galactic rotation, unphysically increasing T_{kmax}; (3) their spin and upper-limit kinetic temperatures can be distorted by uncertainties in the fits because the profiles are sometimes so complicated.

For the WNM in the top two panels, a significant fraction of the WNM gas has $500 < T_{kmax} < 5000$ K, which puts it in the thermally unstable range. $N_{G,WNM} = 14$ WNM components and $N(HI)_{WNM,20} = 11.8$ have $T_{kmax} < 500$ K, so can be classed as too cold to be thermally unstable; these correspond to $(N_{G,WNM}, N(HI)_{WNM,20})$ fractions $(10\%, 4\%)$, respectively. The unstable range has fractions $(39\%, 48\%)$. Even though the lower limits on T_s for some of this gas lie below 500 K, we regard as very remote the possibility that T_s is actually so low because it would require highly supersonic motions. Under this assumption, this is the fraction of WNM gas that truly lies

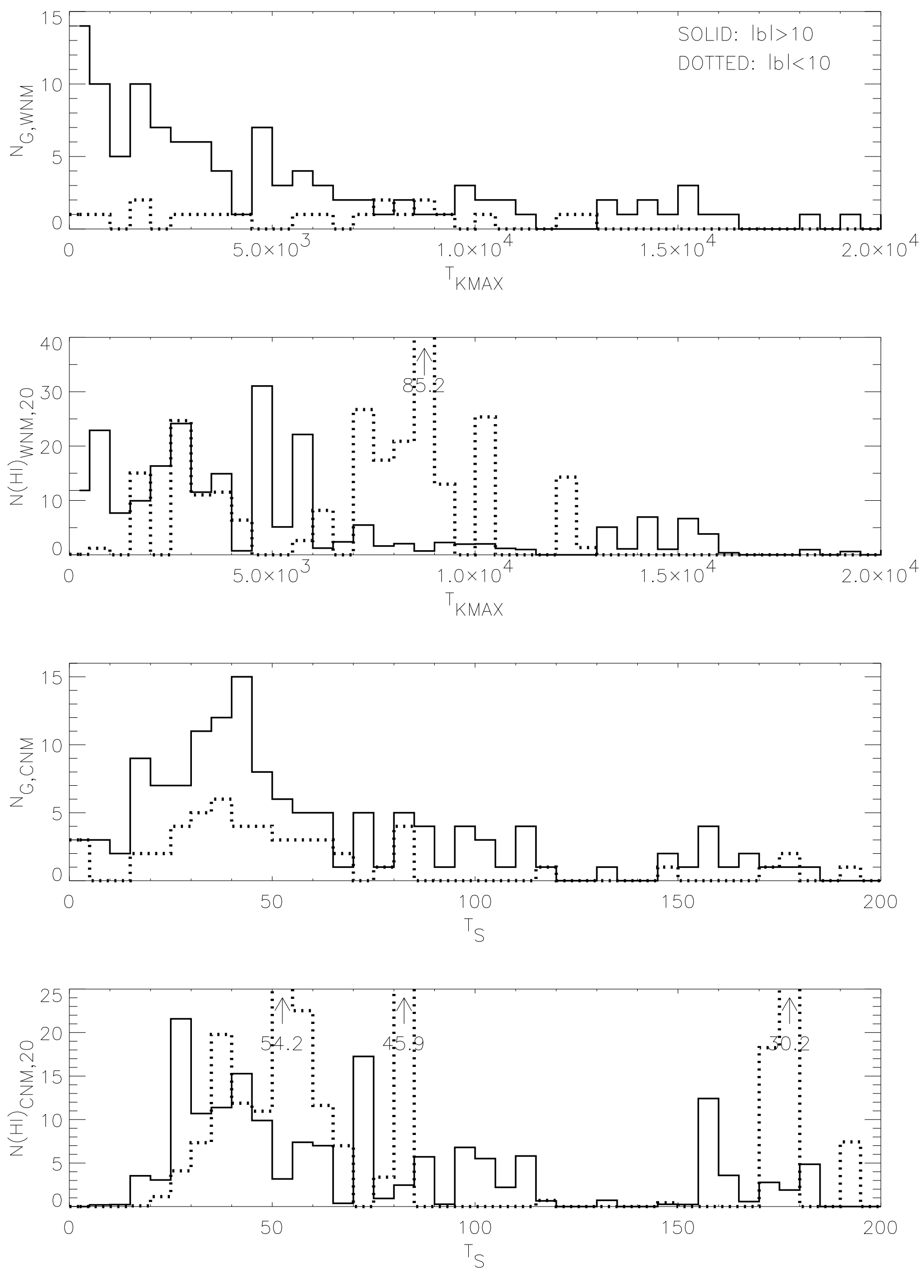

Fig. 2.— Histograms of T_{kmax} for the WNM (top two panels), and of T_s for the CNM (bottom two panels). The solid lines are for $|b| > 10^\circ$ and the dotted ones for $|b| < 10^\circ$. N_G is number of Gaussian components and $N(HI)_{20}$ is column density in units of 10^{20} cm^{-2}.

in the unstable range. Most of the rest $(28\%, 26\%)$ lies between 5000 and 20000 K, and $(23\%, 22\%)$ have $T_{kmax} > 20000$ K and lie off the histograms shown. Any gas having $T_k \gtrsim 10000$ K would be ionized, so components having $T_{kmax} > 10000$ K must either consist of multiple blended narrower components or must have highly supersonic motions.

For the CNM in the bottom two panels, the histograms exhibit well-defined broad peaks near 40 K. Most of the gas $(77\%, 67\%)$ has $T_s < 100$ K. Some of the gas $(17\%, 4\%)$ is very cold, with $T_s < 25$ K; this cannot occur unless photoelectric heating by dust is inoperative (Wolfire et al 1995). In these histograms, the fractions having $T_s > 200$ K and lying off of the histogram are $(8\%, 11\%)$, with the maximum $T_s = 656$ K.

2.2. CNM and WNM combined: distinct populations

Here we address the question of whether the CNM comprises a distinct temperature population. Of course, the CNM is observationally distinguished by its detection in opacity profiles; however, this depends on sensitivity and does not necessarily mean that its belongs to a distinct physical population in the ISM. We restrict our attention to sources having $|b| > 10°$ to minimize the artificial increase of T_{kmax} caused by Galactic rotation and to reduce uncertainties from incorrectly-modeled blended components.

Figure 3 lumps all temperatures, both CNM and WNM, into a single distribution and provides histograms for both number of Gaussian components N_G and column density $N(HI)_{20}$. First consider the first (top) and third panels, which are the histograms of T_{kmax} and T_s for N_G. Both panels exhibit a strong peak towards the left and a long, flat distribution towards the right. These shapes are not suggestive of a continuous distribution, but rather two distributions: one peaked at low temperatures and one spread roughly uniformly over a very broad temperature range running well above 5000 K. The low-temperature peak in T_s for $T_s \lesssim 200$ K is nearly all CNM components; the highest CNM temperature is 656 K. Similar comments apply to panels two and four, which are the histograms for $N(HI)_{20}$, but these histograms are noisier.

We conclude that the CNM is indeed a separate, distinct temperature distribution in the ISM. The median temperature for its Gaussian components is 48 K and for column density 70 K (Table 2), but the histogram in Figure 2 shows large variations. The physical division between the two ISM temperature components is operationally the same as the division between CNM and WNM. However, CNM components lying at high temperatures could also be considered as very cool WNM; the boundary is a bit blurred.

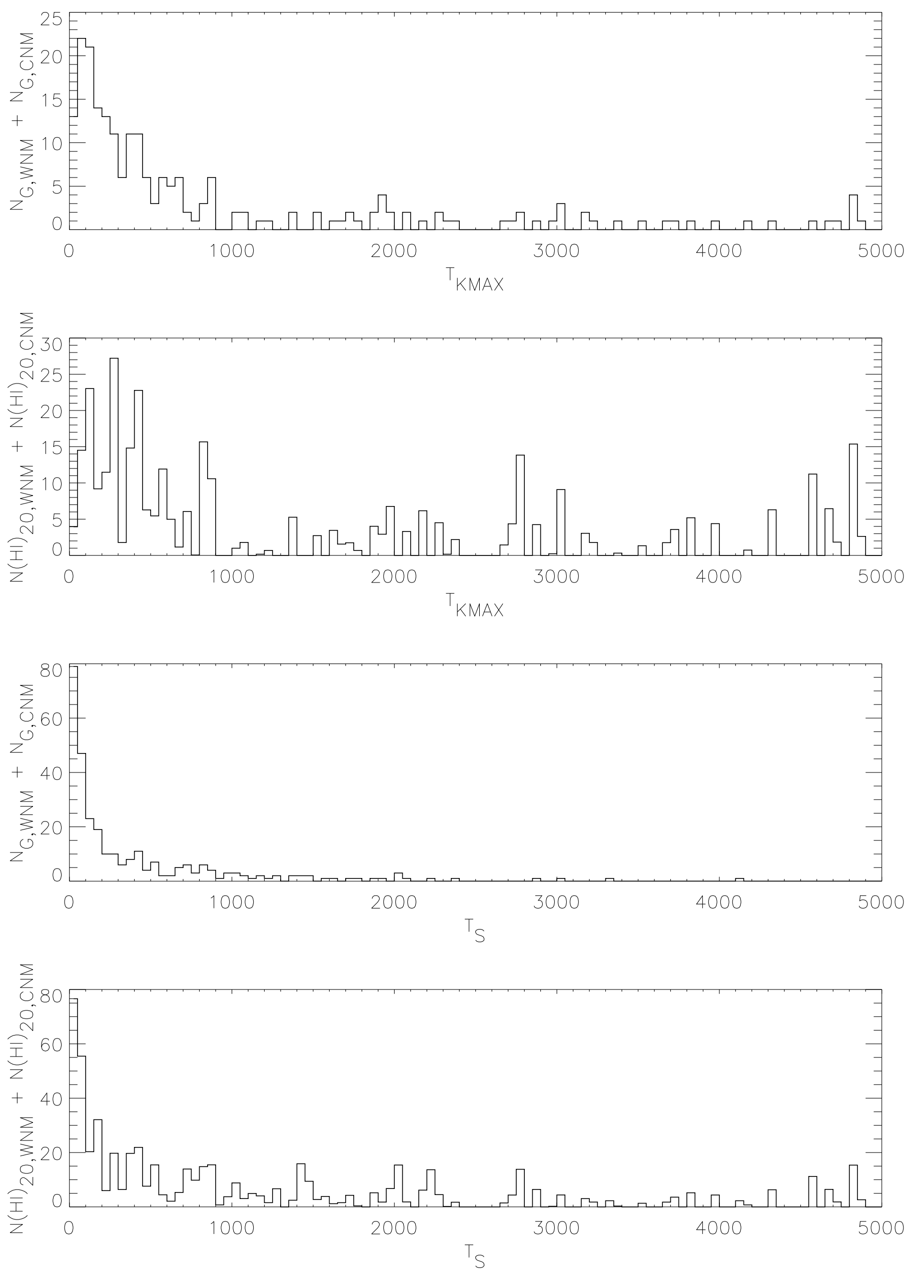

Fig. 3.— Histograms of upper-limit kinetic temperatures T_{kmax} and spin temperatures T_s for the combined set of WNM and CNM components for sources having $b| > 10°$. N_G is the number of Gaussian components; $N(HI)_{20}$ is the column density in units of 10^{20} cm^{-2}. For WNM components, spin temperatures are lower limits.

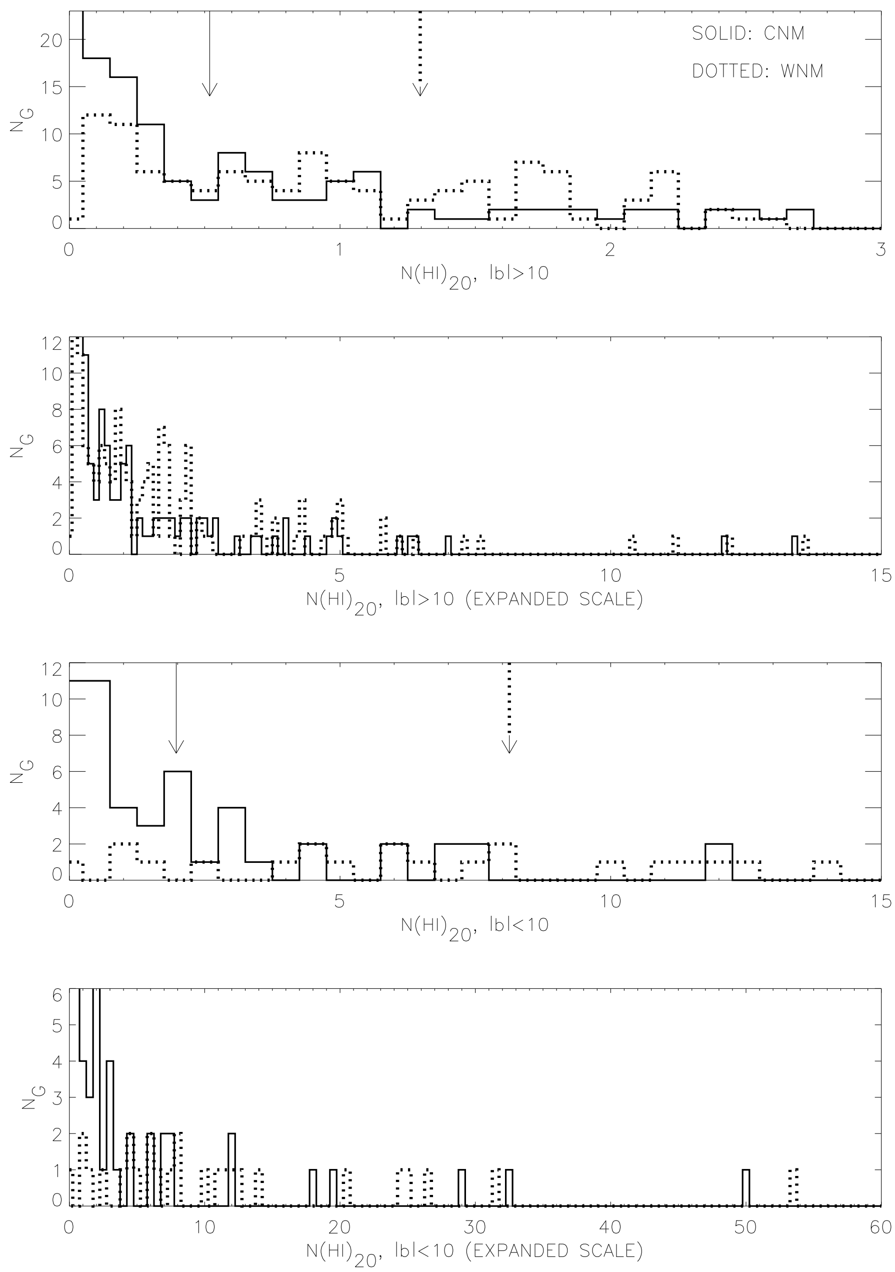

Fig. 4.— Histograms of number of Gaussians N_G and column densities $N(HI)_{20}$ for all Gaussian components, both CNM (solid) and WNM (dotted). The top two panels show $|b| > 10^\circ$ with different scales on both axes to facilitate interpretation; the bottom two panels are for $|b| < 10^\circ$. The arrows show the medians, which are for the (CNM, WNM) (0.60, 1.30) at $|b| > 10^\circ$ and (2.0, 5.0) at $|b| < 10^\circ$. N$(HI)_{20}$ is in units of 10^{20} cm^{-2}.

2.3. Column density statistics for WNM and CNM Gaussian components

2.3.1. Histograms

Figure 4 exhibits separate histograms of $N(HI)_{20}$ for the CNM and WNM Gaussian components. The top two panels show $|b| > 10^\circ$ with different scales on both axes to facilitate interpretation; the bottom two panels are for $|b| < 10^\circ$. Table 3 gives the medians and means. The ranges of column density are enormous, covering more than a factor 100. At low latitudes we see many fewer Gaussian components having $N(HI)_{CNM,20} \lesssim 0.5$, possibly because they are indistinguishable in the presence of blended components at low latitudes.

There appears to be an excess or independent population of low-column-density CNM components having $N(HI)_{CNM,20} < 0.5$; otherwise, CNM and WNM components have similar column density distributions at both high and low latitudes. The similarity of the WNM and CNM distributions for $N(HI)_{CNM,20} > 0.5$ suggests that the two phases could be part of the same population and that members can adopt either temperature range according to circumstances.

2.3.2. Overall summary statistics

For sources at $|b| > 10^\circ$, the global ratio of WNM to total HI column density is $\langle R(HI)_{WNM} \rangle = 0.61$. Mass is equivalent to column density if the distances are the same. The WNM is systematically more distant than the CNM because it has a larger scale height (Kulkarni & Heiles 1987), so this is a lower limit for the mass fraction.

The $N(HI)$ fraction of WNM having T_{kmax} in the unstable region 500 to 5000 K is 0.48; the true fraction of gas in this unstable regime might be higher because T_{kmax} is an upper limit on temperature derived from the linewidth. It's conceivable, but unlikely in our opinion, that much of this gas has temperature $T_k < 500$ K. The $N(HI)$ fraction of CNM having T_s in the range 25 to 70 K (the main peak in the histogram) is 0.46.

At low latitudes, $|b| \lesssim 10^\circ$, the line of sight doesn't leave the HI layer for nearby gas. We can use low-latitude sources as a test to determine whether the fraction of WNM gas $R(HI)_{WNM}$ decreases at lower $|z|$ where the pressure is higher, as is theoretically predicted. We have 8 sources with reasonably accurate Gaussian fits (and 5 with unusable fits; Table 1). These 8 sources have $\langle R(HI)_{WNM} \rangle = (0.67 \pm 0.08)$. This is indistinguishable from the $|b| > 10^\circ$ mean value $\langle R(HI)_{WNM} \rangle = 0.61$. Thus, there is no evidence for the predicted decrease in $R(HI)_{WNM}$. However, we stress that our low-latitude results are generally less accurate than the others because it is more difficult to obtain accurate expected profiles and to perform Gaussian fits. Accurate results for low latitudes probably requires high-sensitivity interferometric observations.

2.4. Comparison of CNM temperatures with other results

Our spin temperatures are colder than previously obtained ones. Histograms of CNM temperatures have been given by Dickey, Salpeter, & Terzian (1978, DST), Payne, Salpeter, & Terzian (1983, PST), and Mebold et al 1982, among others. They find broader histograms than ours with temperatures extending to much higher values and median values in the neighborhood of 80 K. Our histogram is narrower and peaked near 40 K (Figure 2).

The difference does not arise because the older data were incorrect (although some were); it is because the analyses were incorrect. In contrast to the previous treatments, our Gaussian technique, which is thoroughly discussed in Paper I §4 and §5, properly accounts for the two-phase medium and the associated radiative transfer. Recent measurements of temperatures in the Magellanic Clouds (Mebold et al 1997; Marx-Zimmer et al 2000; Dickey et al 2000) use the slope technique, which also properly treats radiative transfer for simple profiles (Paper I, §4, §6); they find smaller temperatures, consistent with ours, and show that the older incorrect technique yields incorrect higher temperatures.

Temperatures are also derived from the ratio of populations in the two lowest rotational states of H_2. Recent FUSE measurements (Shull et al 2000) confirm the large survey of Savage et al (1977), who found the range of temperatures to be $T_{H_2} = 77 \pm 17$ (rms) K. This is much higher than our values. We explore this discrepancy in more detail by considering four of our sources that are fairly close to stars in three regions studied by Savage et al. Table 4 shows radio sources and stars in these three areas; in each area the radio and optical positions are close, within a few degrees. This by no means guarantees that the physical regions sampled are identical, but one hopes that the lines of sight are physically similar. The first two regions have high $N(HI)$ and are cold, with CNM temperatures lying near the peak of our histogram; the H_2 temperatures are higher than the HI temperatures. We detected the 21-cm line in absorption in the third region but we would not classify the 510 K gas as CNM; the H_2 temperature of 377 K is smaller than the HI temperature, although realistic uncertainties may mean that the results are consistent.

The upshot is that the CNM H_2 temperatures do not agree with the HI temperatures. For the CNM having temperatures near our our histogram peak, H_2 temperatures are higher. This could be a result of nonthermal excitation, which certainly operates for the higher-J levels of H_2. These statements need further study and confirmation via observations of HI and H_2 absorption along identical lines of sight. Such observations require a background ssource such as 3C273 with significant radio and UV emission.

In summary, previous 21-cm absorption line studies obtained higher temperatures than we do, but their analyses were flawed and if subjected to proper analyses would probably agree with our temperatures. H_2 temperatures for the CNM tend to be higher than the HI temperatures, and this discrepancy needs further study. We believe that the HI spin temperatures are correct because the 21-cm line is a simple two-level system and its excitation in the CNM is collisionally dominated (Liszt 2001).

3. STATISTICS ON INTEGRATED LINE-OF-SIGHT HI COLUMN DENSITY

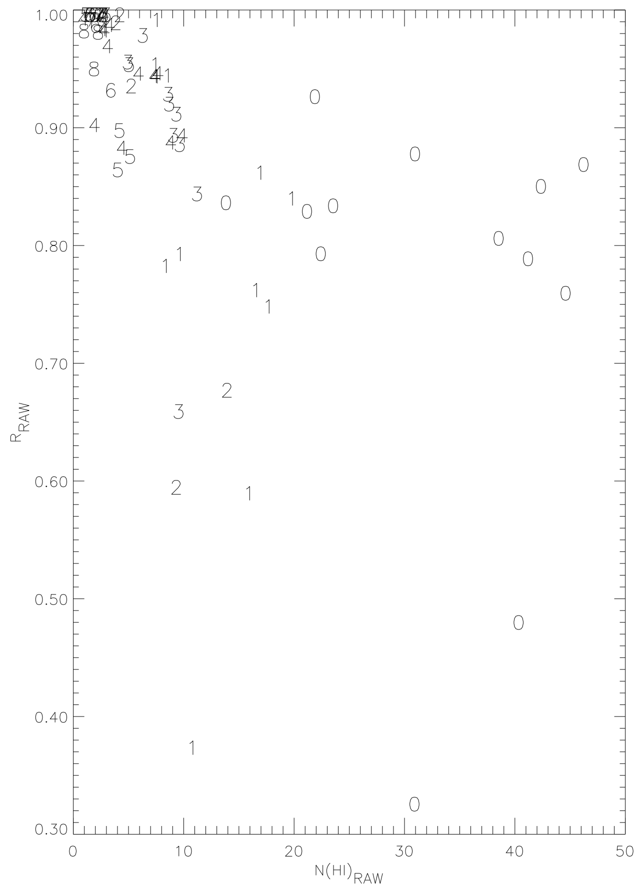

Fig. 5.— Plot of the ratio $R_{raw} = N(HI)_{raw}/N(HI)_{tot}$ versus $N(HI)_{raw}$ for our lines of sight; units are 10^{20} cm^{-2}. This is the factor by which HI column densities obtained from brightness profile integrals are too small. Numbers are $int(|b/10|)$; for example, 3 means $|b|$ lies between 30° and 40°.

3.1. Raw versus true HI column density

One is often interested in the total HI column density. One calculates this from 21-cm line data by assuming that $\tau(\nu) \ll 1$; then $N(HI) \propto$ the profile area. An accurate calculation for the general case requires knowledge of the opacity and the arrangement of the absorbing clouds along the line of sight, which our analysis technique provides. We use our results to compare these two methods.

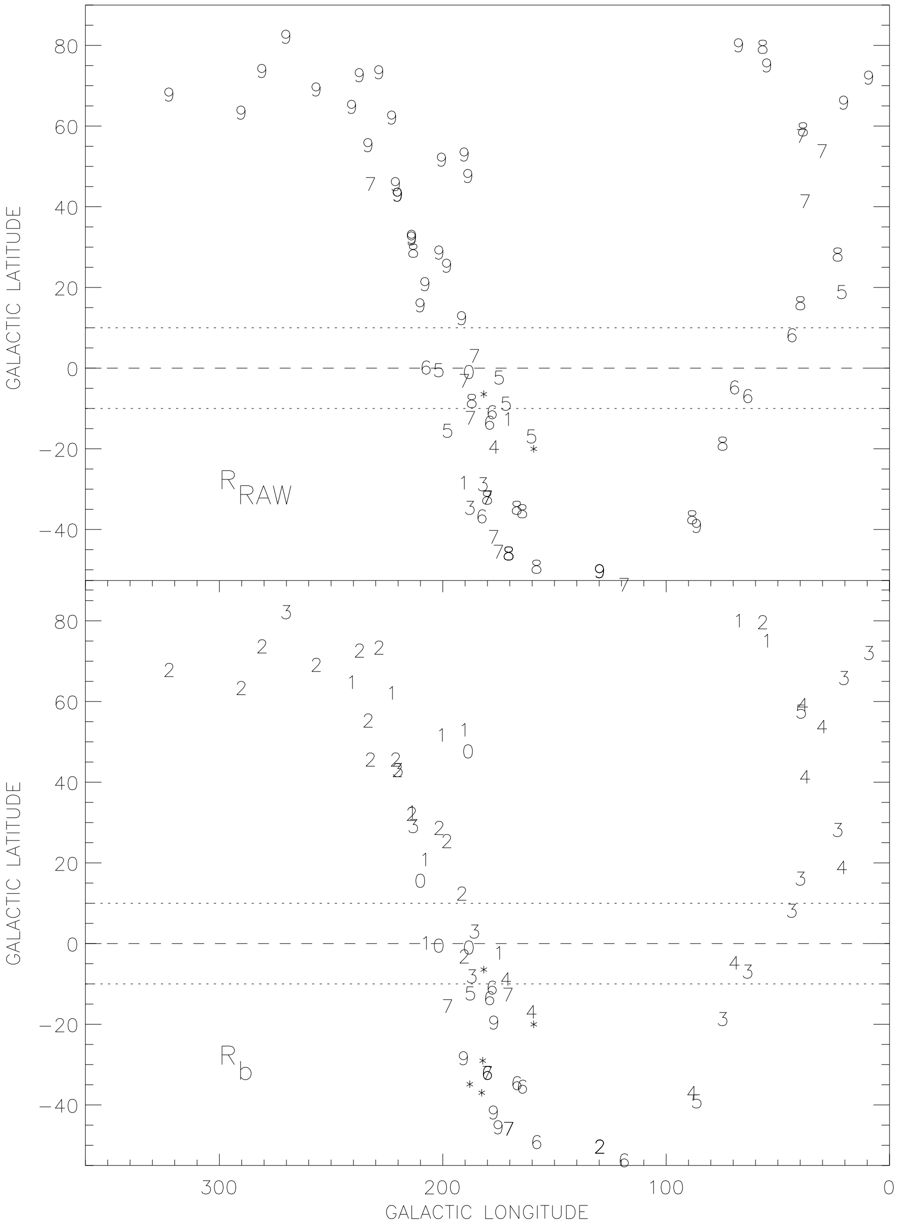

Fig. 6.— *Top*: Map of the ratio $R_{raw} = N(HI)_{raw}/N(HI)_{tot}$ for our lines of sight. Numbers are $int(20(R_{raw} - 0.5)$; for example, 7 means $R_{raw} = 0.85$ to 0.9. *Bottom*: Map of $int(4.5R_b)$, 4.5 times the ratio of actual to total column density expected for a smooth plane-parallel layer in the Galaxy (equation 2). For example, 4 means $R_b = 0.90$ to 1.11. Asterisks mean numbers exceed 9.

We define the "raw" HI column density $N(HI)_{raw}$ as that obtained from the profile area. The true HI column density for a line of sight is equal to $N(HI)_{tot} = \sum N(HI)_{CNM} + \sum N(HI)_{WNM}$, where $\sum$ means summed over all Gaussian components for a line of sight. The ratio

$$R_{raw} = N(HI)_{raw}/N(HI)_{tot} \tag{1}$$

is plotted versus $N(HI)_{raw}$ in Figure 5. Numbers indicate the Galactic latitude $|b|$ in units of 10 degrees. Significant corrections exist, in some cases even at high latitudes and low measured column densities.

Figure 6 (top) shows a map of R_{raw} in which the numbers are $int[20(R_{raw}-0.5)]$; for example, 7 means $R_{raw} = 0.85$ to 0.9. Areas of sky are characterized by R_{raw}. For example, the Taurus/Perseus region ($l = 155°$ to $180°$, $b = -25°$ to $-10°$) has uniformly small values, which is not surprising because of the many molecular clouds and overall high column densities.

3.2. Statistics on line-of-sight HI column densities for $|b| > 10°$

The effect of local structures on total column density is much stronger than the expected latitude dependence. This prevents us from analyzing column density statistics in the usual way of accounting for the expected latitude dependence. In our plane-parallel Galaxy, one classically expects the total column density to be $N(HI)_{20} = 3.7/\sin|b|$ (Kulkarni & Heiles 1987). Define the ratio of the true measured column density to this expected value

$$R_b = \frac{N(HI)_{tot,20}}{3.7/\sin(|b|)} \tag{2}$$

Figure 6 (bottom) is a map of $int(4.5R_b)$; for example, a number 4 means $R_b = 0.89$ to 1.11, so all of the numbers on this map should be equal to 4. Clearly, some areas of sky are deficient and some overabundant.

The top two panels of Figure 7 exhibit the histograms of $\sum N(HI)_{CNM,20}$ and $\sum N(HI)_{WNM,20}$ individually; within the statistics the shapes are not too dissimilar, but the WNM column densities are about twice the CNM ones. The third panel exhibits the histogram for $N(HI)_{tot,20}$; the low-$N(HI)_{tot}$ peak is from the CNM and the tail from the WNM. The fourth panel exhibits the histogram of the CNM column density fraction

$$R(HI)_{CNM} = \frac{\sum N(HI)_{CNM}}{N(HI)_{tot}} \tag{3}$$

for each line of sight.

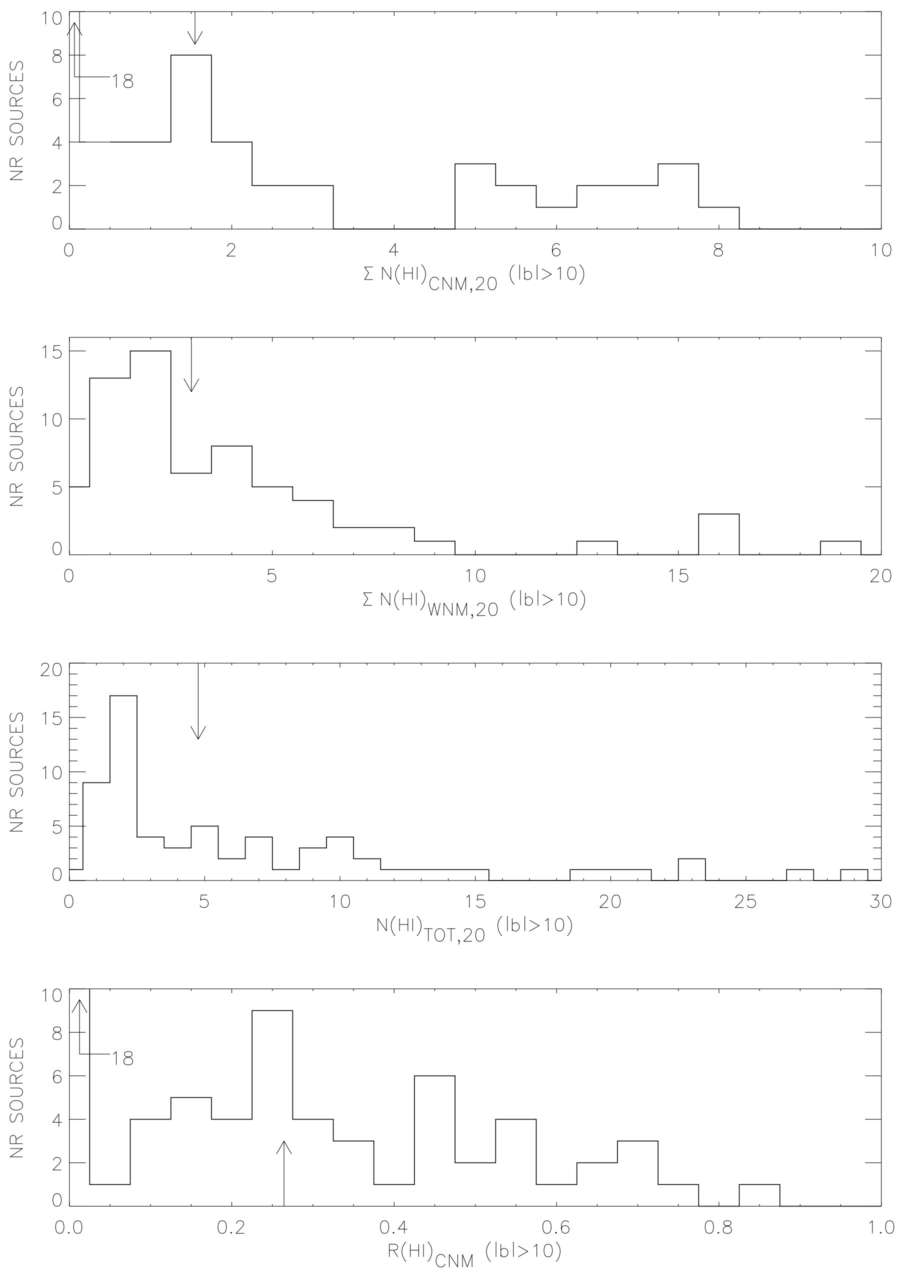

Fig. 7.— Histograms of $\sum N(HI)_{CNM,20}$ and $\sum N(HI)_{WNM,20}$, the total column densities for each line of sight, for sources having $|b| > 10°$. We plot the CNM and WNM individually (top two panels); the total $N(HI)_{tot,20} = \sum N(HI)_{CNM,20} + \sum N(HI)_{WNM,20}$ (third panel), and the CNM fraction $R(HI)_{CNM} = (\sum N(HI)_{CNM})/N(HI)_{tot}$. Arrows show the medians.

The fourth panel, together with the top panel, show a huge peak with zero $\sum N(HI)_{CNM}$. In each case, the peak is distinct from the rest of the histogram. Therefore, lines of sight having zero $\sum N(HI)_{CNM}$ form a *distinct class*. Lines of sight to the majority of sources have $R(HI)_{CNM} \leq 0.3$; however, a few lines of sight are dominated by CNM.

Figure 8 plots $R(HI)_{CNM}$ versus $N(HI)_{tot,20}$, with diamonds for $|b| > 30°$ and plus signs for $|b| < 30°$. The separate class of points with $\sum N(HI)_{CNM} = 0$ is again distinct and mostly has small $N(HI)_{tot}$. Apart from this, a fairly apparent trend is the increase of $R(HI)_{CNM}$ with $N(HI)_{tot}$ up to a limiting $N(HI)_{tot,20} \sim 12$. Surprisingly, this trend levels off, and even seems to reverse, at larger $N(HI)_{tot}$. The points following this reversed trend all lie in the Taurus/Perseus region, where large dust/molecular clouds exist (Figure 9, top).

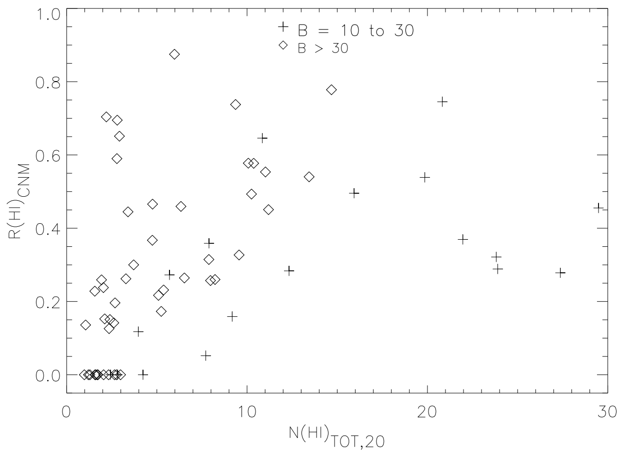

Fig. 8.— The CNM fraction $R(HI)_{CNM} = N(HI)_{CNM}/(N(HI)_{tot}$ versus $N(HI)_{tot,20}$, with low latitudes differentiated from high ones by the diamond and plus-sign symbols. For a map of $R(HI)_{CNM}$, see Figure 9.

Figure 9 (top) shows a map of $R(HI)_{CNM}$ in Galactic coordinates. Points with large and small values of $R(HI)_{CNM}$ tend to cluster. In particular, all but three of the $R(HI)_{CNM} = 0$ points fall in Galactic quadrants 3 and 4 ($\ell > 180°, b > 10°$); this entire region has small values except for the single isolated, unusual point at $(l, b) = (232°, 47°)$. This source, which is 3C237, has one component with $\tau_0 = 0.005$ (which is very small) and $T_s = 656$ K (which is the highest in the sample); it just missed being classed as WNM. If it had been classed as WNM, then 3C237 would have had $R(HI)_{CNM} = 0.30$ and the anomaly would be much less severe. The other three $R(HI)_{CNM} = 0$ points cluster with two others with $R(HI)_{CNM} = 1$ in the upper right of the map.

We conclude that quadrants 3 and 4, and also the upper right of the map of Figure 9 (top), are definitely unusual in having very low fractions of CNM. Both of these regions are disturbed by supershells. Heiles (1998) considers the HI, IR, nonthermal radio continuum, and soft X-ray data

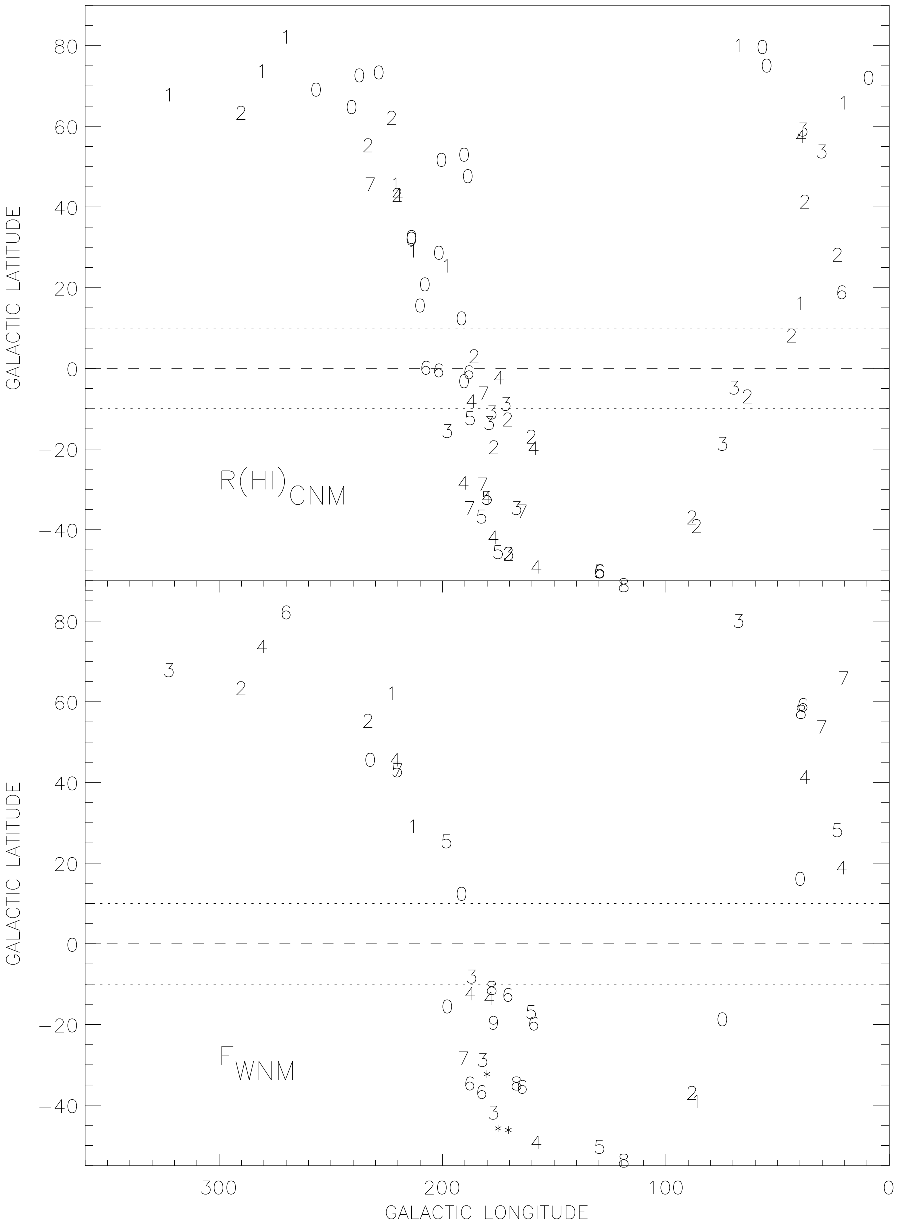

Fig. 9.— *Top*: Map of $int(10R(HI)_{CNM})$, the fraction of CNM to total column density for each line of sight; for example, 0 means $R(HI)_{CNM}$ lies between 0 and 0.1. *Bottom*: For the MO model fits in §9, map of F_{WNM}, the column-density fraction of thermally unstable gas.

and concludes that this general region has been cleared out by a huge superbubble designated GSH 238+00+09, powerful enough to have induced the first stages of star formation in the Vela and Orion regions. Haffner, Reynolds, and Tufte (1998) have discovered a huge Hα-emitting filament that lies in this general region, which may be part of the same superbubble and also related to the unusual values for $R(HI)_{CNM}$. The upper right of the map lies within the North Polar Spur, a supershell produced by multiple supernovae in the Sco/Oph star association (Egger 1998).

4. THE VOLUME FILLING FRACTION OF THE WNM

The WNM constitutes about 61% of the total HI column density for $|b| > 10^\circ$ ($\langle R(HI)_{WNM}\rangle =$ 0.61 (§2.3.2). From large-scale sky surveys the total HI column density, WNM and CNM combined, follows

$$N(HI)_{20} \sim \frac{3.7}{\sin |b|} \tag{4}$$

(Kulkarni & Heiles 1987). Blindly applying our 61% WNM fraction, we obtain for the typical WNM column density

$$N(HI)_{WNM,20} \sim \frac{2.1}{\sin |b|} \tag{5}$$

To progress further we need to adopt a typical temperature for the WNM. From Figure 2, we use 4000 K; this is simply an eyeball estimate of a reasonable value for the purpose of the immediate discussion and is not a median or mean. If the WNM is in pressure equilibrium with the CNM, with $P/k = 2250$ cm^{-3} K (Jenkins & Tripp 2001), then its typical volume density is $n(H)_{WNM} \sim 0.56$ cm^{-3}. Similarly, with the typical CNM temperature of 40 K, the typical CNM volume density is $n(HI)_{CNM} \sim 56$ cm^{-3}. With $\langle R(HI)_{WNM}\rangle = 0.61$, the WNM has about 1.5 times more mass than the CNM and the WNM occupies 150 times more volume than the CNM. These ratios are based on the total column density at $|b| > 10^\circ$ and covers all z heights.

We cannot specify a volume filling fraction for the WNM because our observations are concentrated at $|b| > 10^\circ$ where our lines of sight extend through the top of the gas layer. The total interstellar pressure drops by 30% to 40% from $z = 0$ to 200 pc (Boulares & Cox 1990), so one expects on theoretical grounds that the WNM fraction should increase with z.

We can estimate the volume filling fraction for $z = 0$. However, doing so requires knowing $\langle n(H_2)\rangle$, the mean H_2 volume density at $z = 0$. This is uncertain because it depends on converting CO profile areas to H_2 column densities, which relies on the so-called X factor. Dame et al (1987) used $X = 2.7 \times 10^{20}$ cm^{-2} K km s^{-1} to obtain $\langle n(H_2)\rangle = 0.14$ cm^{-3}; correcting this for the more recent $X = 1.8 \times 10^{20}$ cm^{-2} K km s^{-1} found by Dame, Hartmann, & Thaddeus (2001) gives $\langle n(H_2)\rangle = 0.09$ cm^{-2}. Solomon (personal communication) estimates $\langle n(H_2)\rangle \approx 0.47$ cm^{-3} and

Blitz (personal communication) estimates $\langle n(H_2)\rangle \approx 0.25$ cm^{-3}. We will use the mean of these three numbers, which is 0.27 cm^{-3}, but this is clearly very uncertain. This corresponds to a total H-nuclei column density of 16.7×10^{20} cm^{-2} kpc^{-1}.

We can now estimate the volume filling fraction for $z = 0$. At $z = 0$ the reddening is ~ 0.53 mag kpc^{-1}, which corresponds to $(N(HI) + 2N(H_2))_{20} = 31$ kpc^{-1} (Binney & Merrifield 1998). Of this, the H_2 contributes 16.7×10^{20} per kpc, leaving 14.3×10^{20} cm^{-2} kpc^{-1} for HI. From §2.3.2, we will adopt the tentative $|b| < 1.3°$ value $\langle R(HI)_{WNM}\rangle = 0.61$; thus $N(HI)_{WNM,20} \sim 8.7$ kpc^{-1}, which corresponds to $\langle n(HI)\rangle = 0.28$ cm^{-3}. With a true volume density of 0.56 cm^{-3}, the WNM volume filling fraction ~ 0.50.

This WNM volume filling fraction at $z = 0$, 0.50, is *very rough* because of uncertainties in the following: the accuracy of our low-latitude data; the typical WNM temperature (which we took as 4000 K); the Jenkins & Tripp CNM pressure (Wolfire et al 2002), which we used also for the WNM pressure; the WNM volume density, which is derived from the aformentioned WNM density and temperature; the reddening per kpc; the X factor; and the mean CO profile area in the Solar vicinity. Moreover, it may not apply elsewhere if the Solar vicinity is unusual. In the nearby Solar vicinity the most of the remaining volume is probably occupied by the superbubble HIM as cataloged and crudely sketched by Heiles (1998). The nearby Solar vicinity may have an unusually large fractional volume filled by superbubbles because the average over the disk should be about 0.1 (McKee 1993).

5. STATISTICS ON V_{LSR}

With a good sampling of the sky one could use our Gaussian V_{LSR}'s and Galactic rotation to determine the mean scale heights of the WNM and CNM. However, Arecibo's restricted declination coverage makes our sky coverage too poor for this purpose. Figure 10 shows V_{LSR} versus l for the CNM (top) and WNM Gaussians, together with a 10 km s^{-1} sinusoid to illustrate the expected algebraic sign versus l (the expected amplitude is much smaller). The points exhibit a huge scatter and no tendency to change sign in the expected way. Galactic rotation contributes no recognizable signature to the component velocities.

The standard deviations of the Gaussian component center velocities (i.e., on a component-by-component basis) for the (CNM, WNM) are $\sigma_{VLSR} = (14.0, 16.1)$ km s^{-1}. Weighted by column density, these become $\sigma_{VLSR} = (7.1, 11.4)$ km s^{-1}; the smaller values reflect the fact that higher column density components have smaller σ_{VLSR}, as shown in Figure 11. These column-density-weighted values correspond to FWHM $\Delta V_{FWHM} = (16.6, 26.9)$ km s^{-1} and to $T_{kmax} = (6000, 15900)$ K. The CNM σ_{VLSR} is somewhat larger than the typical WNM sound velocity, indicating that if the CNM consists of clumps moving within a substrate of WNM, then that motion is mildly supersonic unless, perhaps, the WNM is permeated by a magnetic field.

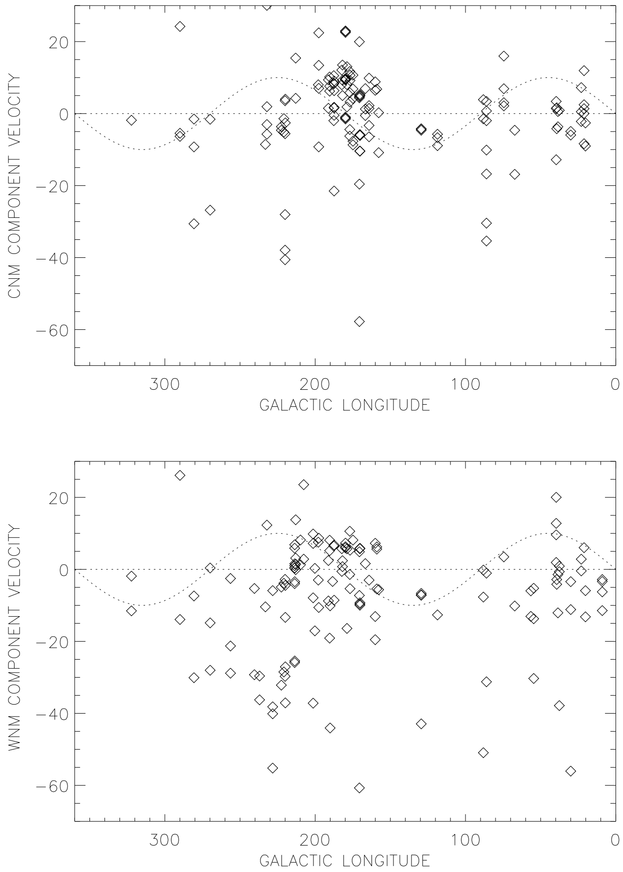

Fig. 10.— V_{LSR} versus Galactic longitude for CNM components (top) and WNM components (bottom), for sources with $|b| > 10°$. The dotted line indicates Galactic rotation with an arbitrary amplitude of 10 km s^{-1}.

6. RELATIONSHIPS AMONG LOGARITHMS OF T_s, τ_0, $N(HI)$, AND T_{kmax} FOR THE CNM COMPONENTS

In this section we discuss correlations among the logarithms of the four CNM parameters $(T_s, \tau_0, N(HI), T_{kmax})$. Significant correlations exist among all pairs of parameters. This is most easily shown in the correlation matrix:

$$\begin{bmatrix} 1.00 & 0.69 & 0.31 & -0.53 \\ 0.69 & 1.00 & 0.38 & -0.40 \\ 0.31 & 0.38 & 1.00 & 0.59 \\ -0.53 & -0.40 & 0.59 & 1.00 \end{bmatrix} \begin{bmatrix} \log T_s \\ \log T_{kmax} \\ \log N(HI) \\ \log \tau_0 \end{bmatrix} \tag{6}$$

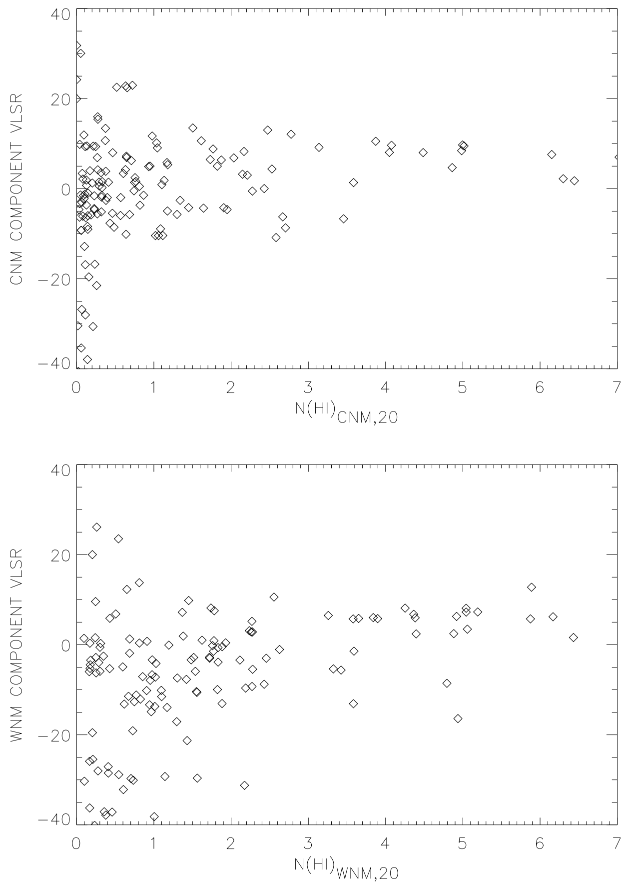

Fig. 11.— V_{LSR} versus $N(HI)_{20}$ for CNM components (top) and WNM components (bottom), for sources with $|b| > 10^\circ$. $N(HI$ is in units of 10^{20} cm^{-2}.

6.1. The Historical τ_0-T_s relationship

Most previous studies of HI opacity [Lazereff 1975, DST, Crovisier 1981, PST] have searched for and found a statistical relationship between the spin temperature and peak optical depth of the form

$$\log(T_s) = \log(T_{s0}) + B\log(1 - e^{-\tau_0}) \tag{7}$$

where temperatures are in Kelvins and we write the equation to explicitly emphasize that the least squares fits are done to the logarithms of the data, not the data. Typically these studies find $[T_{s0}, B] \sim [60\ \mathrm{K}, -0.35]$. The (improper: see below) fit for our data is not dissimilar, yielding $[T_{s0}, B] = [(33 \pm 4)\ \mathrm{K}, (-0.29 \pm 0.05)]$ (we fit $\log(T_s)$ to $\log(\tau_0)$ instead of to $\log(1 - e^{-\tau_0})$; the difference is unimportant because most τ_0 are small). Mebold et al (1982) find no significant relationship. The form of equation 7 has no physical rationale; it is simply a convenient representation of the data. Moreover, τ_0 has no physical influence in the CNM environment so in no case can we regard equation 7 as being causal. On the other hand, PST and Liszt (1983) discuss physical models, involving a cold cloud surrounded by a warm envelope, that lead to reasonable matches with equation 7.

There are two problems with these historical observational results for equation 7. One is that the least squares fits are performed in the conventional way, specifically that the observational errors in the independent variable $(1 - e^{-\tau_0})$ are ignored and implicitly set to zero; this always produces too flat an estimate of the slope (Stetson 2002; Heiles 2002). Thus the typical true slope is more negative than -0.35. Much more serious is the presence of the other two parameters $N(HI)$ and T_{kmax}. Our four parameters exhibit the mutual correlations shown in equation 6. These mutual correlations render meaningless the results of least-squares fits done on only selected pairs of variables. In particular, equation 6 shows that there is no special significance to the (τ_0, T_s) pair because other parameter pairs exhibit similar levels of correlation; the (τ_0, T_s) pair was emphasized in earlier studies because they did not use Gaussian components, so they had no measure of the linewidth T_{kmax} or $N(HI)$.

Even if there were no mutual correlations a τ_0-T_s relationship would occur naturally. Our four parameters are physically related through the usual equation

$$N(HI)_{20} = 0.0195 \tau_0 T_s \Delta V_{FWHM} = 0.0042 \tau_0 T_s T_{kmax}^{1/2} \tag{8}$$

where $N(HI)_{20}$ is in units of 10^{20} cm^{-2} and ΔV_{FWHM} is the FWHM in km s^{-1}. If all clouds have the same or randomly distributed $N(HI)$ and T_{kmax}, then we would expect an inverse correlation between τ_0 and T_s with logarithmic slope -1. When we properly fit this pair of parameters with our data, accounting for uncertainties in both parameters, we obtain $[T_{s0}, B] = [(18 \pm 2)\mathrm{K}, (-0.70 \pm 0.04)]$; the slope is fairly close to -1.[2] Clearly, the τ_0-T_s relationship needs to be considered in the light of a comprehensive multivariate analysis. We revisit the relationship in this light below in §6.3.

6.2. Principal Components Analysis

This is a multivariate data set and an appropriate tool for its investigation is Principal Components Analysis (PCA). For an N-parameter dataset, PCA is a general technique to determine the N different linear combinations of the parameters that express the characteristics of the data

[2]This slope, -0.70, is significantly steeper than the -0.29 derived by ignoring the errors in τ_0, an illustration of the danger inherent in using inappropriate fitting techniques.

more naturally than do the N parameters individually. PCA works using the datapoints themselves, without preconceived notions of what might be significant. Dunteman (1984) provides a good introduction including a graphical illustration for a two-parameter example, while Murtagh & Heck (1987; based on Lebart, Morineau, & Warwick 1984) provides a more thorough discussion, including software.

6.2.1. Quick Description of PCA: the two-parameter example

We present a quick description of the idea for the uninitiated reader. In our case of four correlated parameters, the datapoints fall in a four-dimensional hyperellipsoid, which is somewhat difficult to envision, so we describe an example with only two variables (x, y). The datapoints fall in an ellipse on the (x, y) plane; the principal axes of the ellipse intersect in a center, and they have an axial ratio and slope. These axes are eigenvectors that define the two linear and orthogonal combinations of (x, y) that best represent the datapoint ellipse.

Suppose, as a simple example, that (x, y) represent (luminosity, color) of stars and we look only at main sequence stars with zero reddening. Then the datapoints fall on a line, which is the main sequence, and departures from the line result only from observational errors, which are small but nonzero. Then the longer principal axis of the ellipse represents the main sequence, and its associated eigenvector represents the linear combination of (x, y) that defines the main sequence. The position along this eigenvector is a measure of the stellar mass. The spread (variance) of datapoints along this line is large and represents the range of stellar masses. This illustrates that the eigenvector associated with the largest variance is the most important. The shorter principal axis represents the measurement errors, and the variance along this line is small. In this example, the two eigenvectors have definite and distinct physical meanings. The specification of these eigenvectors, with their minimum and maximum variances, is equlvalent to a least squares fit; when there are more than two parameters, PCA automatically extracts the most significant combinations of parameters (the eigenvectors) for variance maximization.

The real difficulty in PCA is the interpretation. One hopes that the eigenvectors fall into two classes, one with high and one with low variance. The high-variance classes provide physically significant combinations of the original parameters. The low-variance classes provide approximate linear relationships among the original parameters.

In particular, an eigenvector with *zero* variance reveals an *exact* linear relationship among the parameters. In our case, the four parameters are rigorously related by equation 8: the three parameters on the right hand side are determined observationally, and $N(HI)$ is derived from them. Thus the PCA analysis should produce one eigenvector with zero variance and its linear combination of parameters should correspond to the logarithmic form of equation 8. Moreover, if we perform a simultaneous least-squares fit of any one of these four parameters to the other three, we necessarily recover the dependencies in equation 8.

Below we will find that two of our eigenvectors have small variance. This provides two relationships among the parameters. Of course, we will also have two eigenvectors with large variance, meaning that only two linear combinations of parameters are both sufficient and necessary to specify the physical description of a CNM cloud. Because the parameters are all related we have our choice regarding how we actually express these eigenvectors.

If we were to be so fortunate as to find three eigenvectors with low variance, then three of the four parameters would be expressible in terms of the fourth, and CNM clouds would be characterized by only a single eigenvector—a single combination of parameters. In our example of stars above, this is not the case because other parameters such as reddening, metallicity, and age also determine the observable properties of a star. It isn't the case for CNM clouds, either.

In general, the number of eigenvectors must equal the number of parameters. PCA extracts the eigenvectors and their associated variances from the datapoints themselves. For multivariate datasets it is exceedingly useful for exploring fundamental relationships among the parameters. However, it is not a panacea. It cannot deal with differing uncertainties among the datapoints, it cannot derive nonlinear combinations of the parameters, and it cannot provide uncertainties in the derived eigenvectors. Below, we use PCA in combination with least-squares fitting to explore the relationships among our four parameters.

6.2.2. PCA with our four parameters

We applied PCA to our datapoints. As is required for physically meaningful results, we first standardized the measured datapoints by removing means and forcing variances to be equal. Then we performed the PCA. Finally, we reversed the standardization procedure so that we could express the eigenvectors in terms of the original measured parameters.

Fortunately, the eigenvectors do in fact divide into the two classes. The two eigenvectors with large variances are

$$EV1:\ \log T_s + 0.74 \log T_{kmax} + 0.09 \log N(HI)_{20} - 0.41 \log \tau_0 - 3.88\ ;\ variance = 0.52 \tag{9a}$$

$$EV2:\ \log T_s + 1.57 \log T_{kmax} + 4.31 \log N(HI)_{20} + 2.88 \log \tau_0 - 1.88\ ;\ variance = 0.40 \tag{9b}$$

Here we express variances in fractions of the total, so the sum of the four adds to unity; also, the lengths of eigenvectors is arbitrary, and we have arbitrarily made the coefficient of $\log T_s$ equal to unity. For the two eigenvectors having small variances, we set the eigenvectors equal to zero to provide the corresponding equations that relate the parameters. This is strictly valid for the eigenvector $EV4$ with zero variance, but only approximately so for $EV3$:

$$EV3: \ \log T_s = 0.85 \log T_{kmax} - 0.10 \log N(HI)_{20} + 0.006 \log \tau_0 - 0.29 \ ; \ variance = 0.08 \quad \text{(10a)}$$

$$EV4: \ \log T_s = -0.50 \log T_{kmax} + 1.00 \log N(HI)_{20} - 1.00 \log \tau_0 + 2.38 \ ; \ variance = 0.00 \quad \text{(10b)}$$

Equation 10b corresponds exactly to equation 8.

In equation 10a we can ignore the tiny coefficient of $\log \tau_0$, so this equation provides T_s in terms of $[T_{kmax}, N(HI)_{20}]$. This is similar to a least squares fit for T_s in terms of T_{kmax} and $N(HI)$ (see §6.2.4). Alternatively, we can extend the $\tau_0 - T_s$ relationship to include a term in $\log(N(HI))$ by using equations 10 to eliminate T_{kmax}:

$$\log T_s = 0.59 \log N(HI)_{20} - 0.62 \log \tau_0 + 1.39 \quad (11)$$

We hasten to emphasize that we regard this as a mathematical relationship only with no direct physical significance.

6.2.3. *The two fundamental CNM eigenvectors: expressible in two measured parameters*

Finally, we can use equations 10 to eliminate two parameters from the physically significant eigenvectors in equations 9 so as to determine combinations of physically significant cloud parameters. Clearly, τ_0 should be one parameter that is eliminated because it should have no causal influence. Of the three remaining ones, we believe that $N(HI)$ should *not* be eliminated because it is a naturally fundamental quantity that determines the extent to which the cloud interior is shielded from starlight and cosmic rays. This leaves us with the choice of eliminating either T_s or T_{kmax}. It isn't clear *a priori* which is more physically important, so we provide two versions of the two eigenvectors. First, in terms of $(N(HI), T_{kmax})$:

$$EV1: \ 0.41 \log N(HI)_{20} - 0.91 \log T_{kmax} + 4.43 \quad \text{(12a)}$$

$$EV2: \ 0.76 \log N(HI)_{20} + 0.65 \log T_{kmax} + 0.40 \quad \text{(12b)}$$

and next, in terms of $(N(HI), T_s)$:

$$EV1: \ -0.08 \log N(HI)_{20} + 1.00 \log T_s - 1.79 \quad \text{(13a)}$$

$$EV2: \ 0.97 \log N(HI)_{20} - 0.23 \log T_s + 0.68 \quad \text{(13b)}$$

Here we have arbitrarily forced the squares of the coefficients of $\log N(HI)_{20}$ and $\log T_s$ to sum to unity.

Can we interpret these eigenvectors in physical terms? For the first set in equations 12, $[EV1, EV2]$ correspond approximately to $[\left(\frac{N(HI)}{\Delta V^4}\right), N(HI)\Delta V]$. We discern no physical meaning for $EV1$. In contrast, $EV2$ represents the total opacity of the cloud to spectral lines, and we have in mind in particular the CII 157μm cooling line.

For the second set in equations 13, there is a very straightforward physical interpretation for the eigenvectors. The differences between the coefficients of $\log N(HI)_{20}$ and $\log T_s$ are large. Roughly speaking, $EV1$ corresponds to $(\log T_s)$ and $EV2$ to $(\log N(HI)_{20})$. In other words, the two eigenvectors can be taken to be these two parameters instead of two combinations of all four parameters. Writing the two eigenvectors as $[EV1, EV2] = [\log(T_s), \log(N(HI))]$ makes physical sense: T_s makes sense because the CNM cooling time is short, $\sim$ 5000 yr, so the kinetic temperature is a sensitive indicator of the current balance between heating and cooling processes; $N(HI)$ makes sense because colunn density shields the cloud from the external environment and seems equivalent to mass for a star. We conclude that these two parameters—kinetic temperature and HI column density—are convenient, physically meaningful, and approximately orthogonal ones for CNM components.

6.2.4. Least Squares Fits

The relationship of equation 10a comes from PCA, not a least squares fit, so it does not weight datapoints according to their intrinsic uncertainties. Here we perform least squares fits that remove this deficiency. We cannot use conventional least squares fitting because it assumes that the uncertainties in the independent variables are zero. Accordingly, we generalize Stetson's (2002) technique to include multiple independent variables; this is discussed in detail by Heiles (2002).

We take the set of three variables $[\log(T_s), \log(T_{kmax}), \log(N(HI))]$ and perform two independent fits by permuting the independent and dependent variables. These two fits yield

$$\log T_s = (0.87 \pm 0.04) \log T_{kmax} - (0.24 \pm 0.05) \log N(HI)_{20} - (0.27 \pm 0.12) \ \ ; \ \widehat{\chi}^2 = 101 \qquad (14a)$$

and

$$\log T_{kmax} = (1.14 \pm 0.05) \log T_s + (0.27 \pm 0.05) \log N(HI)_{20} + (0.31 \pm 0.12) \ \ ; \ \widehat{\chi}^2 = 101 \qquad (14b)$$

These two different fits provide identical chi-square and, also, self-consistent values for the coefficients and their errors, as they should if the errors in all parameters are properly treated. The reduced chi square $\widehat{\chi}^2 = 101$, which means individual points depart from the fit by typically 10 times their intrinsic uncertainties—the fit should be regarded as a trend instead of an accurate representation of individual datapoints.

We go further by exploring the relationship in the form of equation 14b. We begin our exploration by performing the fits of $\log(T_{kmax})$ to $\log(T_s)$ and to $\log(N(HI))$ independently. These fits yield

$$\log T_{kmax} = (1.32 \pm 0.05) \log T_s - (0.11 \pm 0.13) \;\; ; \; \widehat{\chi}^2 = 117 \tag{15a}$$

$$\log T_{kmax} = (1.11 \pm 0.08) \log N(HI)_{20} + (3.09 \pm 0.05) \;\; ; \; \widehat{\chi}^2 = 902 \tag{15b}$$

The widely different values for $\widehat{\chi}^2$ show that the latter fit, equation 15b, represents the data far less well than the former. Moreover, $\widehat{\chi}^2$ for equation 15a is only marginally worse than that for equation 14b.

We conclude that the trend of variation of T_{kmax} is as well enough expressed by 15a. ssFigure 12 compares graphically the two fits of equations 14b and 15a. The top panel illustrates equation 15a by plotting $\log T_{kmax}$ versus $\log T_s$ and the fitted line. The bottom panel illustrates equation 14b by plotting $\log T_{kmax} - 0.27 \log N(HI)_{20}$ versus $\log T_s$, together with the fitted line. Visually the fits look to be of roughly equal quality, as expected from the comparable values of $\widehat{\chi}^2$.

Equation 15a can be written to express the ratio of total to thermal line widths squared, which is equal to $\frac{T_{kmax}}{T_s}$. This is equivalent to the Mach number of the macroscopic motions ("turbulent" motions) in the cloud:

$$\frac{\Delta V_{tot}^2}{\Delta V_{thermal}^2} = \frac{T_{kmax}}{T_s} = 2.5 \left(\frac{T_s}{40} \right)^{0.32} \tag{16}$$

T_s is typically near 40 K and, moreover, is raised to a relatively small power. Thus, roughly speaking, internal CNM macroscopic nonthermal motions have Mach number ~ 2.5. Because of the large $\widehat{\chi}^2$, individual components differ markedly from this value.

6.3. The τ_0-T_s relationship revisited—and relinquished

Here we revisit the τ_0-T_s relationship by discussing least squares fits on the various parameter combinations $(T_s, N(HI), \tau_0)$. The results of these fits are:

$$\log T_s = (1.25 \pm 0.06) - (0.70 \pm 0.04) \log \tau_0 \; ; \; \widehat{\chi}^2 = 141 \tag{17a}$$

$$\log T_s = (2.45 \pm 0.03) + (0.60 \pm 0.07) \log N(HI)_{20}; \; \widehat{\chi}^2 = 532 \tag{17b}$$

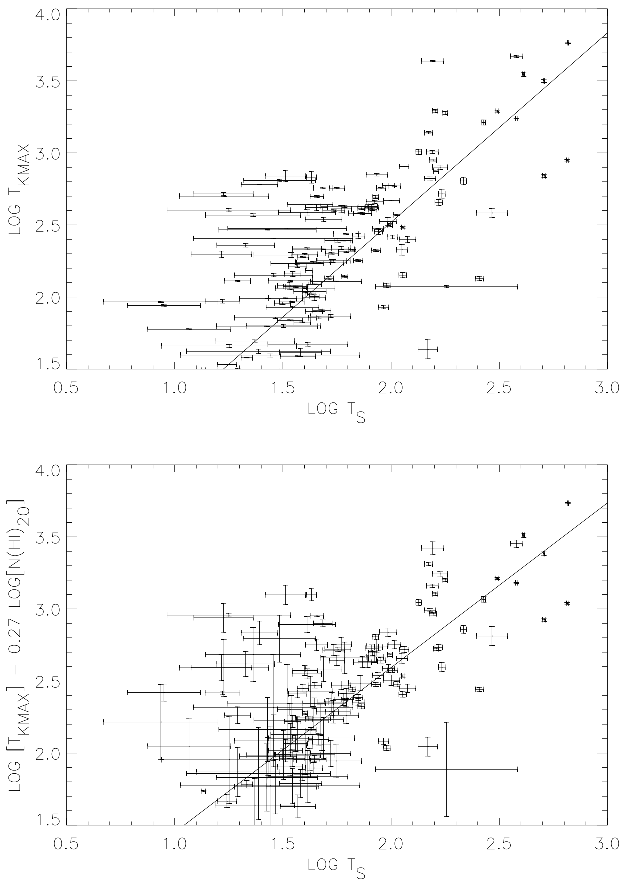

Fig. 12.— Bottom panel: $\log T_{kmax} - 0.27 \log N(HI)_{20}$ versus $\log T_s$, together with the fitted line (from equation 14b). Top panel: $\log T_{kmax}$ versus $\log T_s$, together with the fitted line (from equation 15a.

$$\log T_s = (1.39 \pm 0.01) - (0.64 \pm 0.01) \log \tau_0 + (0.57 \pm 0.01) \log N(HI)_{20};\ \widehat{\chi}^2 = 7.5 \qquad (17c)$$

In contrast to the situation of §6.2.4, the fit that includes both τ_0 and $N(HI)$ provides a far smaller $\widehat{\chi}^2$ than does either of the single-parameter fits. Moreover, the parameters are very well determined. This means that T_s is *not* well-predicted by only τ_0, as is expressed in the classical τ_0-T_s relatinoship.

This good fit is primarily a matter of two relationships:

1. Equation 15a, which is approximate. It relates $\log(T_s)$ and $\log(T_{kmax})$ in an approximately linear fashion, meaning that these two parameters are highly correlated so that, in a least squares fit that included both, the pair would be nearly degenerate. Thus, eliminating $\log(T_{kmax})$ as

an independent variable in a least squares fit has little effect on the quality of a fit for $\log(T_s)$.

2. The logarithmic form of equation 8, which is exact and would produce a perfect least squares fit for $\log(T_s)$ if we included the three other parameters. Not including $\log(T_{kmax})$, which is nearly degenerate with $\log(T_s)$, makes the fit only very good instead of perfect.

We conclude that there is no physically significant τ_0-$N(HI)$-T_s relationship, except as related through equation 8.

7. RAMIFICATIONS OF ISOTROPIC CNM CLOUDS AT KNOWN PRESSURE

Here we discuss the effect of inadequate angular resolution ("beam dilution") on our derived CNM spin temperatures and column densities. We derive physical sizes of CNM components by assuming that the pressure is known. CNM pressures have been measured by Jenkins & Tripp (2001), who find a histogram that peaks near $(P/k) = nT = 2250$ cm^{-3} K, with wide tails. Here we will normalize the ISM pressure in these units, i.e. we write $(P/k) = 2250 P_{2250}$, and normalize the measured temperatures in units of $T_{s,40} = 40$ K, which is close to our histogram peak (Figure 2. We will denote true quantities with a superscripted * and the observed ones with no superscript. For example, the observed spin temperature is T_s and the true one is T_s^*.

7.1. Volume density and size under pressure equality

The column density $N(HI)$ of a Gaussian provides no information on its volume density $n(HI)$ or linear size L. We can obtain these quantities if we know the pressure. Using the parameterization described immediately above, we obtain for the volume density

$$n(HI) = 56 \frac{P_{2250}}{T^*_{s,40}} \text{ cm}^{-3}; \tag{18a}$$

for the length of the cloud along the line of sight

$$L_{||} = 0.57 \frac{T^*_{s,40}}{P_{2250}} N^*(HI)_{20} \text{ pc}; \tag{18b}$$

and, assuming an isotropic cloud, for the angular size,

$$\theta_\perp = 20 \frac{T^*_{s,40}}{D_{100} P_{2250}} N^*(HI)_{20} \text{ arcmin.} \tag{18c}$$

where we normalize the distance to units of 100 pc because this is the approximate scale height of the CNM (Kulkarni & Heiles 1987). Actual distances vary widely; for example, the Taurus complex has distance 140 pc (Arce & Goodman 1999) while the nearby Perseus complex has distance 334 pc (Ladd, Myers, & Goodman 1994).

7.2. Beam dilution and our derived Gaussian parameters

If CNM clouds are isotropic, then those with smallest $N(HI)$ will also have the smallest angular sizes as in equation 18c. These same small clouds may also suffer from beam dilution. Therefore, they will contribute less antenna temperature to our expected emission profiles, and we will derive values of T_s that are too small. This effect can lead to a spurious positive correlation between T_s and $N(HI)$.

Figure 4 shows that $N(HI)_{CNM,20}$ usually lies in the approximate range 0.03 to 1, corresponding to $\theta_\perp \sim 0.3$ to 17 arcmin. The smaller values violate the assumptions inherent in our WNM Gaussian fitting process of Paper I §4.3, where we assume that the CNM clouds contribute to the expected profile with no beam dilution—i.e., we assume that they are large enough to fill the telescope beam of angular diameter ~ 3.3 arcmin (and, more stringently, to fill the beam in the off-source positions, which lie up to 4.5 arcmin away).

To understand this influence, let $N^*(HI)_{CNM}$ and T_s^* be the true values, which are larger than our derived values because of beam dilution. There are two contributions to beam dilution:

1. The ordinary beam dilution that occurs when observing a source whose diameter is smaller than the beam diameter. We express this by the factor F_B, i.e. the factor by which the antenna temperature is reduced by the beam dilution. It obeys (e.g. Rohlfs & Wilson 2000)

$$F_B \sim \frac{(\theta_\perp/\theta_H)^2}{1+(\theta_\perp/\theta_H)^2} \tag{19}$$

   where θ_H is the *effective* HPBW.

2. The increase in effective HPBW caused by our use of off-source observations to define the cloud's antenna temperature. This is fully discussed in Paper I, §3.5. If a cloud is larger than Arecibo's 3.3 arcmin beam but smaller than the angular offsets for the off-source spectra, then the derived emission antenna temperature from the cloud is too small. This use of off-source data increases the innate 3.3 arcmin HPBW to the effective one. This effective HPBW should be roughly equal to the square root of the sum of the squares of the innate HPBW and the angular displacement of the off-source positions (about 5 arcmin). That is, the effective HPBW is about 5.7 arcmin. Accordingly, we define the effective HPBW to be

$$\theta_H = 5.7 F_H \text{ arcmin} . \tag{20}$$

where F_H is a factor, close to unity, that more exactly defines the correct effective HPBW. F_H depends on things such as the exact cloud shape and the intensity distribution within the cloud boundary.

By combining equations 18c and 20, we find that beam dilution becomes significant for $(\theta_\perp/\theta_H) \lesssim 1$, which occurs for $N^*(HI)_{CNM} \lesssim 0.3\frac{D_{100}P_{2250}F_H}{T^*_{s,40}}$. For this case, we simplify the following equations by substituting for equation 19 the much simpler equation

$$F_B \sim (\theta_\perp/\theta_H)^2 \ . \tag{21}$$

In terms of physical quantities of equation 18c this becomes

$$F_B \sim \left(\frac{T^*_{s,40}}{D_{100}P_{2250}F_H}\frac{N^*(HI)_{CNM,20}}{0.3}\right)^2 \tag{22}$$

The observed spin temperature T_s and column density $N(HI)_{CNM,20}$ are both directly proportional to the antenna temperature, so they are reduced by the same factor:

$$T_s = F_B T^*_s \tag{23a}$$

$$N(HI)_{CNM,20} = F_B N^*(HI)_{CNM,20} \tag{23b}$$

Combining the previous three equations, we obtain F_B in terms of observed instead of true parameters

$$F_B \sim \left(\frac{T_{s,40}}{D_{100}P_{2250}F_H}\frac{N(HI)_{CNM,20}}{0.3}\right)^{2/5} \tag{24}$$

Suppose, for purposes of illustration, that all correlation coefficients are zero except between T_s and $N(HI)$. Then a least squares fit between these is meaningful and produces the result $\log T_s = 2.45 + 0.60N(HI)_{20}$, i.e. $T_{s,40} = 7.0N(HI)_{20}^{0.60}$. This is, of course, a relation between the *observed* parameters. Using this observed relation together with equations 22 and 23 to express a new relation in terms of the *true* parameters, we obtain

$$T^*_{s,40} = 1.7(D_{100}P_{2250}F_H)^{0.44}N^*(HI)_{CNM,20}^{-0.11} \tag{25}$$

It is surprising to see that, while the *observed* relation has a *positive* slope, the *true* relation has a *negative* slope. This illustrates that beam dilution is important and can drastically affect the relationships among observed quantities. Historical studies that obtained expected profiles with larger telescope beams than Arecibo's include Lazereff (1975) and Mebold (1982).

However, we emphasize that beam dilution effects are much less severe than we calculate here. Recall that our analysis applies only in the case $N^*(HI)_{CNM,20} \lesssim 0.3\frac{D_{100}P_{2250}F_H}{T^*_{s,40}}$, a criterion based on the assumption of isotropic clouds expressed quantitatively in equation 18c. However, we argue in §8 that CNM components are sheetlike, not isotropic. Therefore, they are much more extended in the plane of the sky than predicted by equation 18c, and beam dilution effects are correspondingly much smaller.

8. EVIDENCE AGAINST ISOTROPIC CNM CLOUDS

If CNM clouds are isotropic, then we predict in §7.1 (equation 18c) the approximate angular size of CNM clouds. In particular, all values for T_s and $N(HI)_{CNM}$ are affected by beam dilution when $N^*(HI)_{CNM,20}\left(\frac{T^*_{s,40}}{D_{100}P_{2250}}\right) \lesssim 0.3$. Here we test this prediction using five pairs of our sources that are closely-spaced and, also, using previous observations in the literature. We find that CNM clouds are extended over much larger angles than predicted by equation 18c. Indeed they are often so extended that they appear much more sheetlike than isotropic.

8.1. Evidence from our own data

Table 5 lists CNM Gaussian parameters of common components for our five closely-spaced source pairs. For each pair, the parameters for each source are given in fractional form together with the ratio. For each individual Gaussian component, we list the derived $N(HI)_{CNM}$ and also the area under the Gaussian function fit to the opacity profile. We believe it is better to compare profile areas. The area is derived directly from the opacity profile, while $N(HI)_{CNM}$ is less accurate because it contains the error in derived T_s, which contains the error obtained from combining the opacity profile and the expected profile. The expected profile is subject to the additional uncertainties discussed in Paper I §5.2. These are particularly serious for weaker opacity components, which are just the ones we are interested in.

For the pair 3C225a/3C225b we list only the strongest opacity component. From the opacity profiles, one sees that both sources have two much weaker components in common centered near $V_{LSR} = (-5.6, -2.8)$ km s^{-1}. These were included in our fit for 3C225b but not for 3C225a because of the large uncertainty in the opacity profile for 3C225a and our criteria for fitting Gaussians explained in Paper I §5. Visually the two opacity profiles look similar, and if we had included them it would bolster our case that opacity components don't change rapidly with position.

Scanning Table 5, we see no little tendency for ratios to depart from unity more with decreased column density. Moreover, even for low column densities the components not only exist for both pair members, but the ratios usually don't depart too far from unity—only two of the AREA ratios exceed 2. Even for the 3C310/3C315 pair, separated by nearly 2°, the ratios are quite close to unity. This is contrary to the basic prediction of the raisin pudding model. The 3C225a/b pair, and in addition the source 3C237, constitute a special case.

8.2. The 3C225a,b and 3C237 "Triad Region"

The source pair (3C225a, 3C225b) and also 3C237 all have a similar opacity component which is prominent in the expected and the surrounding emission profiles, offering us a unique opportunity to map a CNM opacity component. 3C237 is about 9° away from the 3C225a,b pair. The 3C225a,b component was noticed long ago and partially mapped in emission as "Cloud A" by Knapp and Verschuur (1972). The region they mapped shows an elongated cloud, at least 5° long and about 1° wide; they didn't complete the map and, in particular, didn't carry it far enough north to include 3C225a and 3C225b. They derived the spin temperature by assuming the intrinsic line shape to be Gaussian and fitting for the saturation; they found $T_s \approx 24$ K over the whole of the cloud. They also mapped "Cloud B", which is associated with 3C237 and is similarly cold.

In fact, components similar to these clouds exist over tens of square degrees in the region centered near $(l, b) = (225°, 44°)$. We used the Leiden-Dwingeloo survey of Hartmann and Burton (1997) to map this feature, exploring the entire positive-latitude region within the range $l = 200°$ to 240°. On line profiles, the feature is a sharp narrow peak on the side of a much broader one, as in our expected profiles for these sources. To locate positions containing the feature, we sharpened each profile by subtracting from each profile its 3-point median-filtered counterpart. Then we least-squares fit the narrow feature plus a constant and slope and rejected solutions having small slopes and large widths. We confirmed the suitability of this procedure by visual inspection of the profiles.

Figure 13 exhibits the results. Within the region surveyed we found the feature to exist only within the smaller region shown; it is possible that the feature extends beyond $l = 240°$. The left column of panels are maps of the three Gaussian parameters height, center velocity, and width for this cloud, which has V_{LSR} decreasing slowly from ~ 4 to 2 km s^{-1} as l increases to the left across the map. The right column shows a much less predominate but similar feature which has V_{LSR} decreasing from ~ 0 to -8 km s^{-1} as l increases from the map center towards the left.

The predominant component appears as three clouds forming a ribbon of width $\sim 2°$ and length $\gtrsim 20°$. While the ribbon is interrupted by voids, the coherence of its characteristics indicates strongly that it is the really the same physical feature. With its temperature $T_s \sim 25$ K and typical $N(HI)_{CNM,20} \sim 0.3$, the volume density $n(HI) \sim 90 P_{2250}$ cm^{-3} and $L_{||} \sim (0.11/P_{2250})$ pc. In contrast, the length across the line of sight is $L_{\perp} \sim 30 D_{100}$ pc. The aspect ratio is

$$\frac{L_{\perp}}{L_{||}} \sim 280 D_{100} P_{2250} \tag{26}$$

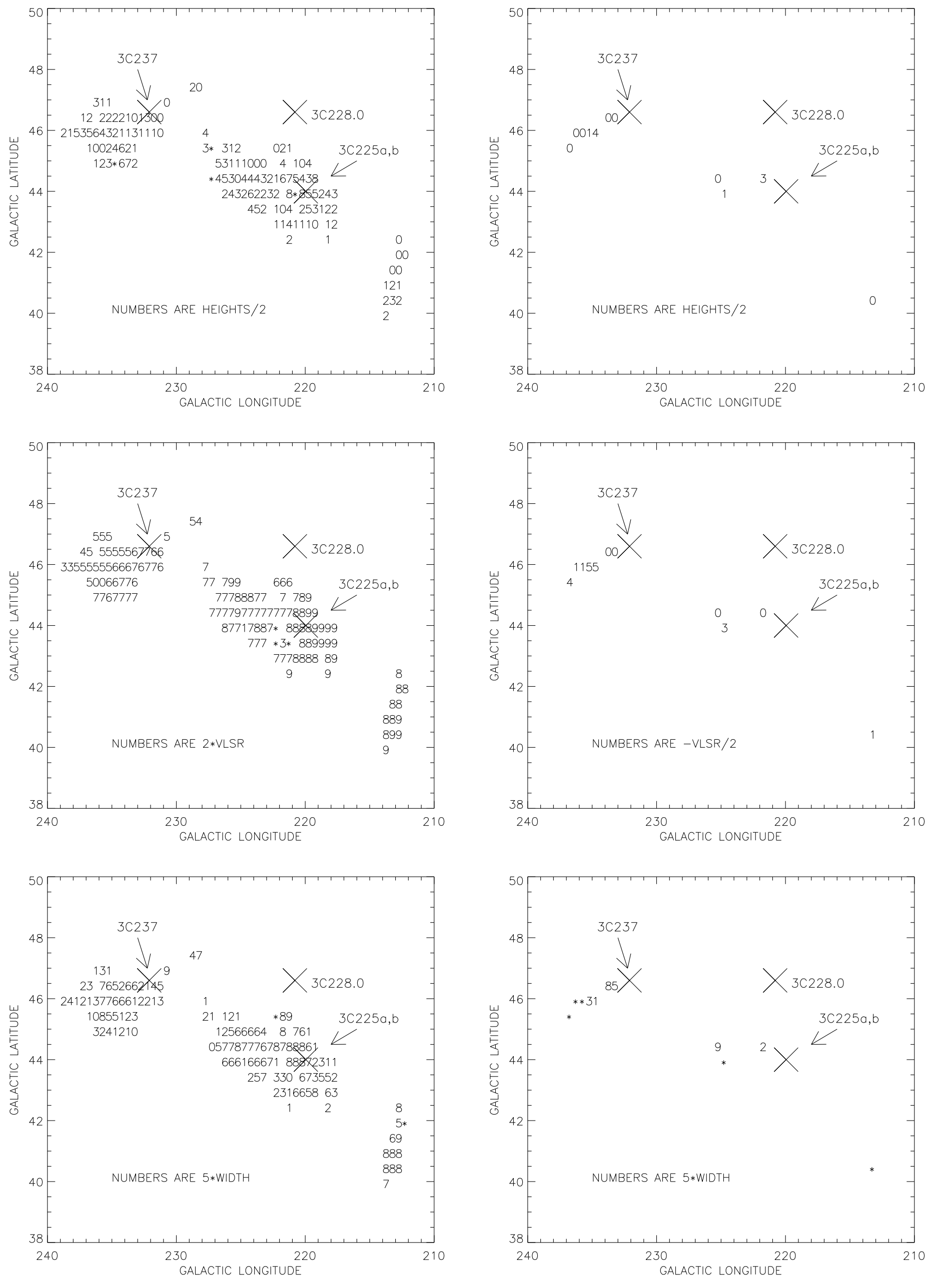

Fig. 13.— Maps of cold gas ($T_s \sim 25$ K) towards $(l, b) = (225°, 44°)$. Left column shows the predominant component at $V_{LSR} \sim 4$ km s^{-1} and the right the less predominant one at $V_{LSR} \sim -4$ km s^{-1}. The top row shows Gaussian peak height, the center row the V_{LSR}, and the bottom row the halfwidths. Each single-digit number represents a half-degree pixel.

which is comparable to the aspect ratio for, say, an old-fashioned LP record.

The occasional presence of the negative-velocity feature is intriguing. The velocity difference at the positions where it exists ~ 5 km s^{-1}. If these two features were the opposite sides of an expanding shell, then the expansion velocity would be too small to create a shock in WNM gas. Moreover, both V_{LSR}'s are small. If the feature had been produced by a higher-velocity shock and slowed to its current V_{LSR}, then inhomogeneities in the ISM would produce significant variations in the current V_{LSR}, which don't exist. It seems unlikely that the sheetlike structure results from a shock front.

8.3. The "Small Region" of Heiles (1967)

For his particularly well-conceived thesis, Heiles (1967) used the mighty NRAO 300-foot telescope to map the 21-cm line in a ~ 160 deg^2 region centered on $(l, b) \sim (120°, 15°)$. The HI profiles in this region are characterized by two narrow peaks sitting on a broad underlying component. In some of the region, the underlying component has $T_{kmax} \sim 2500$ K. For the two peaks, he estimated the ΔV_{FWHM} to be ~ 3.3 km s^{-1}, which corresponds to $T_{kmax} \sim 240$ K. These components must be CNM. This is confirmed by the detection of 21-cm line absorption against the sources 4C78.01, 4C72.01, 4C74.08, and 4C76.13 in the huge Nançay survey of Crovisier, Kazès, and Aubry (1978).

Heiles maps these CNM components, so here we have another rare opportunity to view the angular structure of CNM. His Figure 7 shows maps of the two peaks. The maps show narrow rifts running through otherwise large-scale and rather lumpy distributions. The rifts can only occur if these structures are sheets. The velocities merge near one end of the region, from which Heiles concludes that they are physically related and could easily be the front and rear walls of an expanding shock.

The high-velocity sheet (HVS) is lumpier and has $N(HI)_{CNM,20}$ ranging up to ~ 4; the low-velocity sheet (LVS) is smoother with smaller peak columns, about 2.5. Thus these sheets have about ten times the column density of the triad region's sheets discussed in §8.2. For these sheets Heiles estimates $L_{||} \lesssim 3.6 T_{40}/P_{2250}$ pc. On the plane of the sky, $L_{\perp} \sim 50 D_{100}$ pc, so

$$\frac{L_{\perp}}{L_{||}} \gtrsim 14 \frac{D_{100} P_{2250}}{T_{s,40}} \tag{27}$$

Heiles estimates $D_{100} \sim 5$, so $(L_{\perp}/L_{||}) \sim 70$; this ratio is not as spectacularly high as the triad region sheet but is nevertheless quite impressive.

Heiles also finds "cloudlets" within the sheets and summarizes their statistical properties in his Figures 11 and 12. The areal density is high: 815 cloudlets over 160 deg^2 is 5 per deg^2, or half this for each sheet. The ΔV_{FWHM} histogram is narrow, ~ 0.8 km s^{-1} wide, and peaked at ~ 2.0 km s^{-1}, corresponding to $T_{kmax} = 88$ K. The median column density $N(HI)_{CNM,20} \sim 0.3$, much like the sheets in the Triad Region; this gives $L_{||} \sim 0.17 T_{s,40}/P_{2250}$ pc. The typical angular diameter is 31 arcmin, so the cloudlets have

$$\frac{L_\perp}{L_{||}} \sim 4.9 \frac{D_{100} P_{2250}}{T_{40}} \; . \tag{28}$$

With $D_{100} \sim 5$, these are also very sheetlike, but not so much as the sheets with which they are associated.

The term "blobby sheet" seems to be the correct descriptive term the large sheets in the Small Region.

8.4. Evidence from other studies

High-resolution studies of the CNM provide abundant evidence that the CNM is not distributed in isotropic clouds. On large scales, the maps of HI in self-absorption by Gibson et al (2000) and Gibson (2001) show a plethora of structures. Commenting on their Figure 1, Gibson et al (2000) describe it as including "overlapping knots, filaments, and other complex structures." The low-latitude gas studied by them is quite distant, so these structures are hundreds of parsecs in scale. Other, more localized studies of the CNM, outlined below, also reinforce the conclusion that the CNM does not lie in isotropic clouds.

Greisen and Liszt (1986; GL) made interferometric high-resolution (a few arcsec) maps of the 21-cm line opacity spectra against the extended sources 3C111, 3C161, and 3C348. They examined the angular structure of 9 Gaussian opacity components. Obtaining $N(HI)_{CNM}$ for their components requires assuming T_s; if $T_s = 40$ K, then $N(HI)_{CNM,20}$ ranges from 0.20 to 2.0. Two of the three sources had $|b| < 10°$, so many components have $D_{100} \gg 1$. Nevertheless, the fluctuation statistics of all 9 components are similar, approximately independent of $N(HI)_{CNM}$. GL found variations on scales $\gtrsim 30$ arcsec; they characterize those variations as "well-behaved", meaning that the variations are relatively smooth and not disorganized or chaotic. Thus, the CNM Gaussians do not display the random polka-dot pattern expected from the independent clouds.

GL do see one cloud edge. Their lowest-$N(HI)_{CNM,20}$ $(= -0.20)$ component resides towards 3C161 $[(l, b = (215.4, -8.1)]$ and has $V_{LSR} = 28$ km s^{-1}, making $D_{100} \sim 28$. Equation 18c predicts $\theta_\perp \sim 0.08$ arcmin. In fact, they saw this component in only two of three positions; the two positions are separated by 0.15 arcmin, and the third is 0.9 arcmin away, so the cloud is larger than we predict by at least a factor of two. However, this is not a very serious discrepancy; it can be fixed by adjusting P_{2250} and/or $T_{s,40}$.

GL analyzed two components in 3C348, which is also on our source list. The results are given in Table 6. The stronger V_{LSR} 0.5 km s^{-1} component has a larger fractional variation in profile area than the weaker one, which is contrary to our expectation from §7.2.

Dickey (1979) analyzed pairs of opacity spectra against lobes of double radio sources. Two, 3C348 and 3C353, have $|b| > 10°$. 3C353 has a strong opacity component (we find $\tau_0 = 1.2$) which shows less than 10% variation across 3.7 arcmin. He resolved 3C348's opacity spectrum into two components, one at $V_{LSR} = 0.1$ and one at 7.9 km s^{-1}; the former is strong (our $\tau_0 = 0.6$) and has $\lesssim 7\%$ variation and the latter is weak (our $\tau_0 = 0.078$) and has $\lesssim 30\%$ variation across 1.9 arcmin. In a related study PST compared the properties of opacity spectra against small-diameter and large-diameter (up to a few arcmin) sources and found no statistically significant differences. These results are a bit marginal in sensitivity but do reinforce our conclusion.

Kalberla, Schwarz, and Goss (1985) used the WSRT to generate a high-resolution HI data cube centered on 3C147, located at $(l, b) = (161.7°, 10.3°)$. They were able to map the emission produced by five Gaussian components in the opacity profile over their field of view, which is about 30 arcmin diameter. In every case the emission has structure on the scale of a few arcmin but is extended and spills outside the field of view in at least one direction. This is a very direct way to study the angular extent of the CNM and needs to be repeated for many sources.

8.5. Summary: CNM component morphology must be sheetlike

The above comparisons of opacity profiles using both our own data and previous literature show that the rapid angular variation in opacity profile structure expected under the isotropic cloud model does not occur in the sources studied. These sources are not a complete sample and these comparisons should be extended. Nonetheless, not a single source with HI absorption nor any HI line survey supports the isotropic cloud model for the CNM. That is, equation 18c does not correctly predict the scale of angular variations in CNM clouds.

Equation 18c is based on three assumptions.

1. The CNM pressure $P_{2250} \sim 1$. This pressure is observationally determined from observations of the CI line, which is produced in CNM regions. It has a significant dispersion but a well-defined median. This assumption is as close to an observational fact as we get in astronomy.

2. The distance $D_{100} \gtrsim 1$; if a cloud becomes arbitrary close, then it can have arbitrarily large $\theta_\perp$. We observe from within the Local Hot Bubble (LHB), which has a radius $\sim$ 50 to 150 pc, depending on direction (Sfeir et al 1999). The LHB is characterized by its pervasive HIM and absence of dense clouds. Our CNM components cannot be produced within the LHB, so they cannot lie arbitrarily close.

3. Clouds are isotropic so that $L_\perp \sim L_{||}$. This assumption must be wrong. The maps for the Triad and Small Regions are specific cases, with aspect ratios in the range 100-300, where this assumption clearly does not apply. Another is the recent maps of 21-cm line self-absorption in the Galactic plane (Gibson et al 2000, Gibson 2001), which show structures with all angular

scales and even a blobby sheetlike structure extending over many degrees (because it is distant, this means hundreds of parsecs).

The maps for the Triad and Small Regions are specific cases for which the isotropic assumption does not apply, as are the low-latitude regions mapped by Gibson et al (2000) and Gibson (2001). We conclude that CNM clouds are not isotropic. To reproduce the observed situation in which they almost always extend over much larger angles than the $\theta_\perp$ of equation 18c, they must be sheetlike. The sheets are not perfectly smooth because we do see variations with position. They are best characterized as "blobby sheets".

In §7.2, we discussed the effects of beam dilution on the derived spin temperatures and column densities for isotropic clouds. However, clouds are not isotropic, so the effects estimated there are greatly exaggerated. Nevertheless, these effects probably do operate at some level because the CNM sheets are blobby.

9. A DIRECT COMPARISON WITH THE McKEE/OSTRIKER MODEL

The McKee and Ostriker (1977; MO) model of the interstellar medium predicts each CNM component to be embedded in, and thus pressure equilibrium with, a single WNM cloud. The WNM acts as a buffer between the cold, neutral, dense gas and the X-rays produced by the Hot Ionized Medium (HIM), cosmic rays, and UV radiation from stars. Most of the WNM envelopes should be in thermally stable equilibrium with $T_k \sim 8000$ K.

9.1. Method and tabular results

We directly investigate the applicability of the MO model to our data by performing least-squares fits with this model directly in mind. In contrast to our empirical method described in Paper I §5, which models the WNM as a small number of Gaussians with arbitrary centers and widths, here we model the WNM as follows:

1. We begin with the same CNM components as in Paper I.
2. One portion of the WNM, the CNM-associated portion, is represented by a set of WNM Gaussians, each WNM Gaussian having the same central velocity as its corresponding CNM component. We assume that the WNM components have no significant nonthermal motions, so we constrain the width to be $T_{kmax} = T_k = 8000$ K. We allow departures from this constraint as described below.
3. The other portion of the WNM, the CNM-independent one, is represented by one, or in a very few cases two, additional Gaussians, with arbitrary centers and widths, that are unrelated to

the CNM components. The MO model allows this because not every WNM cloud need have a CNM core; and our data demand it.

This model is surprisingly successful at fitting many of our profiles. However, for many sources the fit is significantly improved by allowing allow departures from assumption (2) as follows:

4. Sometimes CNM components are spaced so closely, i.e. much closer than the WNM linewidth $\Delta V_{FWHM} = 19$ km s^{-1}, that the associated WNM components are degenerate. In these cases, we use a single WNM component for all of the closely-spaced CNM components and in statistical discussions divide the WNM equally among the associated CNM components; thus all of these CNM components have the same WNM column density, which we denote by the symbol $N(HI)_{WNM;CNM}$, but of course they have different CNM column densities $N(HI)_{CNM}$. We always try to pair a WNM component with each CNM one. However, if this doesn't work, we define a CNM component to be associated with a WNM component if the CNM's velocity falls within the halfwidth range of the WNM Gaussian.

5. Sometimes it is obvious that the fit can be greatly improved by allowing the WNM line width to vary as a free parameter. This allows us to derive values for T_{kmax} for the WNM components that differ from 8000 K. Almost all of these have lower T_{kmax}, and many of these lie in the unstable region between 500 and 5000 K.

6. Almost always, a small change in WNM line center has little influence on the fit quality. This is in contrast to the line width, mentioned above. 3C274.1 is the only case where a change in WNM line center would significantly improve the fit, but we we don't allow the central velocity to change because we wish to keep the model as simple as possible without generalizing it for a single exception. This has no significant effect on the derived values of T_{kmax} and no ramifications for our discussion.

Except for 3C133, 3C409, 4C13.67, and P0531+19, we excluded sources having $|b| < 10^\circ$ from the analysis because the profiles are too complicated. We also excluded all sources having no CNM components. This leaves a total of 47 sources with 112 WNM components and 142 CNM components. 82 of these 112 WNM components are associated with the 142 CNM ones, and 30 WNM components are not associated with CNM.

12 good-quality fits follow the MO model strictly in having one-to-one paired WNM and CNM components plus perhaps an additional CNM-independent WNM component. Including multiple CNM components per WNM component, 38 sources have good quality fits. 3 sources, 3C142.1, 3C225b, and 3C274.1 have poor quality fits, but no worse than for the standard fits. The fits for 5 sources were much worse than the standard fits: 3C207, 3C315, 3C318, 3C409, and P0428+20. 3C225b also falls into this category, but only because some narrow opacity components are not represented by Gaussians because of its large error in the opacity profile.

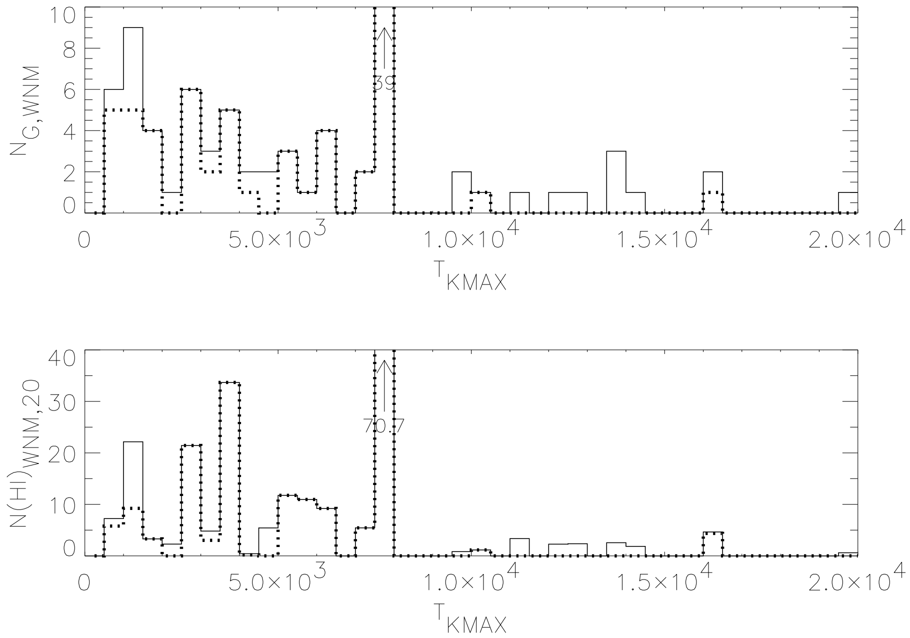

Fig. 14.— For the MO model fits, histograms of T_{kmax} for the WNM Gaussians of the MO-fit model. The dotted histogram shows CNM-associated WNM components and the solid histogram all WNM components. The top histogram is for number of components N_G and the bottom one for $N(HI)_{WNM}$. Annotated arrows indicate histogram heights for all WNM Gaussians at $T_{kmax} = 8000$ K, only one which is not associated with CNM; it contains $N(HI)_{WNM,20} = 1.0$.

9.2. Linewidths, T_{kmax}, CNM and WNM column densities

9.2.1. Thermally unstable WNM

For CNM-associated WNM components, we allowed the linewidth T_{kmax} to vary as a free parameter if this would significantly improve the fit. For many sources this adjustment was not required. When it was required, the resulting T_{kmax} was almost always less than 8000 K. The fact that most fits did not require this adjustment and that sometimes the line width is smaller suggests that the temperature 8000 K is, indeed, a reasonable one for much of the WNM, as predicted by MO and subsequent theory (e.g. Wolfire et al 1995) and, moreover, that nonthermal line broadening is not very important in much of the WNM (in contrast to the CNM).

Figure 14 shows histograms of T_{kmax} for the WNM components, both the CNM-associated ones (dotted histogram) and all WNM components (solid), and both for number of components N_G and for $N(HI)_{WNM}$. The obvious peaks at $T_{kmax} = 8000$ K result from CNM-associated WNM where we have constrained the WNM linewidth by this temperature [see (2) in §9.1 above].

WNM gas components that are not associated with CNM ones were, of course, fit without a width constraint. Some gas [(7%, 6%) for ($N_G, N(HI)$)] has $T_{kmax} > 20000$ K and is off the histogram to the right. Apart from the 8000 K peak, the histogram is not dissimilar in shape to the corresponding histograms in Figure 2.

Much of the CNM-associated WNM gas, (35%, 40%) for number of components and column density, lies in the thermally unstable range 500 to 5000 K; the corresponding fractions for all WNM gas are (34%, 41%). For our standard fits these fractions were (39%, 48%) (§2.3.2). These column density fractions are comparable, which suggests that these numbers are robust. The sources analyzed here are only those containing CNM components, which is a biased sample, so we adopt the higher value from §2.3.2 as our final one and conclude that a significant fraction of all WNM, $\gtrsim 48\%$ by mass, lies in the thermally unstable range 500 to 5000 K.

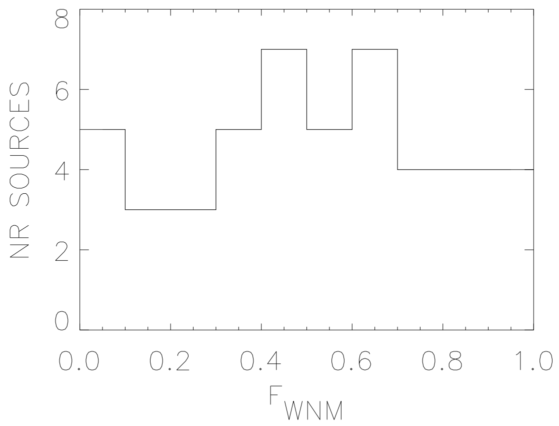

Fig. 15.— For the MO model fits, histogram of F_{WNM}, the column-density fraction of all WNM along a line of sight that has T_{kmax} in the thermally unstable range 500 to 5000 K.

Consider the fraction F_{WNM} of all WNM gas along a line of sight that lies in the thermally unstable range 500 to 5000 K. Figure 15 shows a histogram of this ratio. The distribution is roughly flat, with no preference for any particular ratio. Figure 9 (bottom) shows a map of this quantity; the highest values seem to cluster in the Taurus-Perseus and NPS regions. This suggests a correlation between F_{WNM} and $R(HI)_{CNM}$. The correlation coefficient is 0.29, but the scatter plot is not very impressive to the eye. We conclude that thermally unstable gas is common and not closely related to other physical parameters.

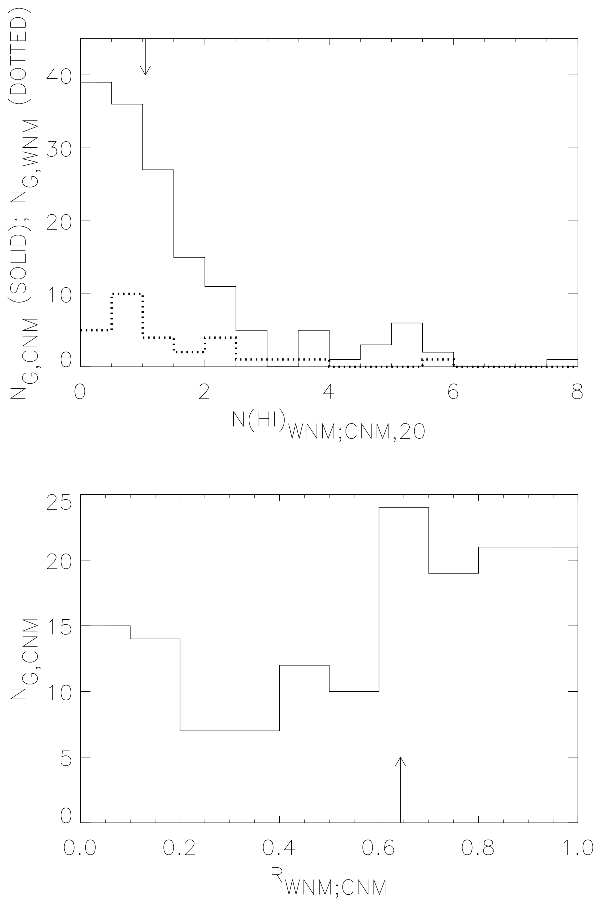

Fig. 16.— For the MO model fits. *Top*, the solid line is the histogram of $N(HI)_{WNM;CNM}$, the total WNM column density associated with each CNM component; the dotted line is the histogram of WNM *not* associated with CNM (for which the horizontal axis should be labeled $N(HI)_{WNM,20}$). $N_{G,CNM}$ is the number of CNM Gaussian components. *Bottom*, histogram of $R_{WNM;CNM}$ for each CNM component. See §9.2.2 and §29.

9.2.2. Fraction of WNM gas

The MO model predicts the WNM column density associated with a CNM core, which we define as $N(HI)_{WNM;CNM}$; this notation is meant to mirror that of conventional statistics, i.e. the WNM column density given a certain CNM one. It is calculated as described in (2) and (4) of §9.1. Figure 16 shows two histograms of $N(HI)_{WNM;CNM}$. The bottom panel shows the fraction

$$R_{WNM;CNM} = \frac{N(HI)_{WNM;CNM}}{N(HI)_{WNM;CNM} + N(HI)_{CNM}} \ , \tag{29}$$

which is, for a particular CNM component, the ratio of its associated WNM column density to total CNM-associated column density (both WNM and CNM).

The MO model predicts that every CNM cloud is enveloped in WIM and that some, $\sim 1/3$, are also enveloped in WNM. MO Figure 1 shows a typical small cloud, which has with typical total column densities through the diameter $N(HI)_{WNM,20} \sim 0.03$ and $N(HI)_{CNM,20} \sim 1.3$. This gives $R_{WNM;CNM} \sim 0.02$. These numbers are very rough, but do not agree at all with the observational data in Figure 16.

This disagreement is simply a different expression of the large WNM fraction in the ISM, which disagrees with the MO model. The MO model predicts a much smaller ratio of WNM to CNM column densities than we observe, whether or not we fit our observations in terms of the MO model or with the empirically oriented method of Paper I. Overall, MO predict that less than 4% of the diffuse interstellar gas should be WNM. Yet here and in §3 the ratio is much larger. The overall ratio of all WNM to total for this MO-oriented fit, whether or not the WNM is associated with CNM, is $R(HI)_{WNM} = 1 - R(HI)_{CNM} = 0.57$, which is more than ten times what MO predict. For the entirety of sources treated using the empirical method of Paper I, $R(HI)_{WNM} = 0.61$. This latter number is a bit higher and is better because the MO-model sample is restricted and biased.

9.3. Summary of comparison with MO

The data compare with the MO model in the following respects:

1. Modeling WNM profiles as envelopes having the same velocity as their associated CNM Gaussians works very well for most sight lines, but for some it works poorly.

2. The WNM column densities in the CNM envelopes are far larger than predicted.

3. Overall, the WNM constitutes about 61% of the total HI, more than ten times the predicted fraction.

4. At least $\sim 48\%$ of the WNM is thermally unstable. MO would allow only a small fraction, that portion of the gas that is transiting from one phase to another.

10. TWO DESCRIPTIVE MODELS BASED ON OBSERVATIONS

10.1. The raisin-pudding model: not applicable

First we discuss the CNM statistics in terms of the often-used conceptual model of randomly distributed isotropic clouds embedded in a WNM substrate, which we term the "raisin-pudding" model. This model is popular and deserves to be addressed, despite the fact that we have shown in §8 that CNM clouds are not isotropic.

For purposes of discussion we will suppose that the WNM has typical $T_k = 4000$ K; if $T_k = T_{kmax}$ this is not an unreasonable discussion value, and is convenient because it is 100 times our adopted CNM temperature. If the WNM has the same pressure as the CNM, then its volume density is 100 times smaller. Our $N(HI)$ histograms show that the WNM column density $N(HI)_{WNM}$ is typically larger by a factor ~ 1.5 than $N(HI)_{CNM}$. This makes the typical ratios $L_{||,WNM}/L_{||,CNM}$ and $\theta_{\perp,WNM}/\theta_{\perp,CNM} = 150$ (for definitions, see §7.1).

Suppose that both the CNM and WNM consist of isotropic clouds of diameter $L_{||,CNM}$ and $L_{||,WNM}$, respectively. The CNM Gaussian component clouds are much smaller than the WNM ones, so we imagine that the CNM clouds are embedded in a single WNM Gaussian component cloud of diameter $L_{||,WNM}$—like raisins in a giant pudding. The number of CNM components that should be observed along a typical line of sight is $N_{CNM} \sim (L_{||,WNM}/S_{||,CNM})$, where $S_{||,CNM}$ is the mean free path for a line of sight intersecting the CNM clouds. The mean free path is

$$S_{||,CNM} = \frac{1}{\sigma_{CNM}} \tag{30}$$

where σ_{CNM} is the effective cross section of the cloud; for a spherical cloud, the effective size is the diameter plus the diameter L_O of the sampling beam (which can be the radio source for absorption and the telescope beam for emission), so

$$S_{||,CNM} = \frac{4}{\pi\left(L_{||,CNM} + L_O\right)^2} \tag{31}$$

The number of CNM clouds per unit volume is

$$\nu = \frac{4N_{CNM}}{\pi L_{||,WNM}\left(L_{||,CNM} + L_O\right)^2} \tag{32}$$

and the total number of CNM clouds residing within the WNM cloud is

$$\mathcal{N} = \frac{2N_{CNM}}{3}\frac{\left(L_{||,WNM}/L_{||,CNM}\right)^2}{\left[1 + (L_O/L_{||,CNM})\right]^2} \tag{33}$$

This number is enormous. For $N_{CNM} > 1$ and $(L_{||,WNM}/L_{||,CNM}) = 150$, it exceeds 2×10^4.

10.2. The CNM clumpy sheet model: better

The ISM contains more WNM than CNM. The are many lines of sight that contain WNM but no CNM. The WNM is extended over path lengths of 100 pc or more. This does not require or even suggest the MO concept in which each CNM cloud has a separate, independent WNM envelope; if this were the case in fact, then with just a few CNM components their associated WNM envelopes would merge into a single WNM cloud. This points towards a model in which the WNM occupies large volumes and CNM components lie inside.

From §8 we find that the CNM components are sheetlike. From §8.4 we find that the CNM sometimes appears as elongated filaments. A continuous, wrinkled sheet can look like a filament where the sheet happens to lie tangent to the line of sight (Hester 1987). Also, a thin ribbon can also be perceived as a filament.

If all CNM sheets had the same column density thickness, then the observed $N(HI)_{CNM}$ would increase as the sheets become more tangent to the line of sight. With a random distribution orientation large tilt angles are preferred, so the histogram of $N(HI)_{CNM}$ should increase markedly towards large values. Figure 4 shows that it doesn't. This means that the intrinsic column density thickness has a wide dispersion: some sheets are thin, some are thick. In two regions for which we are fortunate enough to have CNM maps, the CNM is distributed in huge blobby sheets of thickness ~ 0.11 and $\lesssim 3.6$ pc, with length-to-thickness aspect ratios ~ 280 and ~ 70.

If these characteristics are general, then the CNM seems to be organized into a small number of large, thin structures. In contrast to the raisin pudding model, in which the CNM blobs are spherical and randomly distributed with $\gtrsim 2 \times 10^4$ CNM cloudlets within a WNM cloud, there are only a few such sheets. The sheets probably contain lots of blobs; in the Small Region the density ~ 2.5 cloudlets per deg^2, or 1 cloudlet per 30 pc^2. This is conceptually a much different morphological arrangement than the raisin pudding model.

The arrangement in large sheets is consistent with ideas that the CNM forms from large-scale shocks produced, for example, by supernovae or large-scale vertical shocks (Walters & Cox 2001). The Small Region's sheets merge in velocity and are suggestive of what we expect from an expanding shell, and were originally so interpreted.

However, invoking a shock for the Triad Region has its difficulties. First we remark on a favorable situation for the shock interpretation, namely the cold temperature ($T_s \sim 20$ K), which suggests an absence of grain heating, and the grains could have been destroyed by the shock. The sheet's V_{LSR} is small, suggesting a shocked shell that has suffered substantial deceleration. But the velocity fluctuations are also small, which is unexpected because the deceleration should occur in a clumpy medium, producing large velocity fluctuations. In particular, we would expect large fluctuations for a sheet with small column density, which is the case here ($N(HI)_{CNM,20} \sim 0.3$).

This clumpy sheet model must be considered provisional because it is based on extrapolating mapping results from only two regions to the entire ISM. We desperately need CNM maps for more regions. New maps of self-absorption of the 21-cm line in the Galactic plane are being produced by the current interferometric HI surveys, e.g. Gibson et al 2000. Maps away from the Galactic plane are also important because they allow detailed study of regions with less confusion caused foreground/background gas.

11. SUMMARY

Paper I discusses the observational and data reduction techniques. In particular, it devotes considerable attention to the Gaussian fitting process, which is subjective and nonunique. Concerned readers should see §5 of that paper.

The present paper treats the astronomically oriented implications of the Gaussian components from Paper I and includes the following topics:

1. §2.1 discusses the statistics of the Gaussian components. It shows that the CNM and WNM are not only observationally distinct, but also physically distinct. The median column density per CNM Gaussian component is about 0.5×10^{20} cm^{-2}, and per WNM component about 1.3×10^{20} cm^{-2} (Table 3).

   The CNM temperature histogram peaks near $T_s = 40$ K (Figure 2), about half the temperature obtained by previous workers. CNM temperatures range down to ~ 15 K, which can be attained only if grain heating is not operative. CNM temperatures appear to be smaller than those derived from UV absorption line observations of H_2, but we have no common lines of sight and cannot make direct comparisons.

   A significant fraction of the WNM, $\gtrsim 48\%$, lies in the thermally unstable range $T_k = 500$ to 5000 K.

2. §3 summarizes the statistics of WNM and CNM column densities for entire lines of sight instead of individual Gaussian components. There are many lines of sight having no CNM; these form a distinct class and are confined to particular areas of the sky. Column densities depart very markedly from those expected from a plane-parallel distribution. 61% of the HI we observed is WNM; at $z = 0$, it fills $\sim 50\%$ of the volume, but this number is *very rough.*

   Figure 5 shows the factor R_{raw} by which $N(HI)$ calculated from the optically thin approximation (i.e. from the line profile area) underestimates the true $N(HI)$; this can be significant even at high Galactic latitudes.

3. §5 shows that the component velocities that we observe are not significantly affected by Galactic rotation. The column-density weighted rms velocities are about 7 and 11 km s^{-1} for the CNM and WNM Gaussian components, respectively.

4. §6 uses Principal Components Analysis, together with a form of least squares fitting that accounts for errors in both the independent and dependent parameters, to discuss the relationships among the four CNM Gaussian parameters. The spin temperature T_s and column density $N(HI)$ are, approximately, the two most important eigenvectors; as such, they are convenient, physically meaningful primary parameters for describing CNM clouds.

   The Mach number of internal macroscopic motions for CNM clouds is typically 2.5, but there are wide variations. We discuss the historical τ_0-T_s relationship in some detail and show that it has little physical meaning.

5. §7 discusses the possible effect of angular resolution on the relationships among observed CNM parameters. These effects are important if CNM clouds are isotropic. However, §8 shows that CNM clouds are definitely not isotropic. CNM features are sometimes large sheets with aspect ratios measured in the hundreds. These sheets contain blobs, which themselves are sheetlike but with much smaller aspect ratios.

6. §9 directly compares our data with the McKee/Ostriker model by re-reducing all Gaussian components in terms of that model, i.e. with each CNM cloud having an associated WNM envelope. This fitting scheme works very well for many sources, but not for all. The MO model greatly underpredicts the WNM abundance and, also, the fraction of WNM that is thermally unstable.

7. In §10 we argue that there is so much WNM that CNM clouds probably don't have individual WNM halos, but rather that many CNM clouds exist within a common WNM halo. We discard the raisin pudding model as a commonly envisioned descriptive model and replace it by the blobby sheet model, in which the CNM consists of sheetlike structures with sheetlike blobs or cloudlets embedded within. Each WNM cloud probably contains a few CNM large sheets.

8. §8 uses our knowledge of the CNM pressure to derive the morphological shape of CNM structures: they are sheetlike. In two regions of the sky the CNM is organized into large sheets with length-to-thickness aspect ratios ~ 280 and 70; the latter is permeated by small sheetlike structures.

9. In the following section we provide comments on the importance of the WNM for understanding not only the ISM but also the full range of its energy sources.

12. THE WNM: KEY TO THE UNIVERSE

From the theoretical standpoint, Wolfire et al (1995; WHMT) show that the temperature of the CNM is well constrained: if the density is large enough, the time scale for equilibrium is short and the equilibrium temperature is well defined. Their predicted temperature is close to the peak in our CNM histogram, so our data are very consistent with their results. Anomalies with colder temperatures such as the Triad Region's sheets can be achieved if grain heating does not operate; these regions are fascinating, but not very common.

The WNM is another matter. Theoretically, the temperature is well constrained, but the time scale for equilibrium is not short. Moreover, there are formally forbidden ranges in density and temperature because of the thermal instability. In fact the thermal time scales are long enough that a sufficiently chaotic medium might never reach thermal equilibrium. Theories like WHMT's that discuss only the thermal equilibrium microphysics cannot easily deal with these matters.

Our finding that much of the WNM lies in the thermally unstable range 500 to 5000 K strongly implies that thermal equilibrium does not, in fact, obtain for much of the WNM. Moreover, the WNM seems to have significant ionization, with a mean ionization fraction possibly as high as 0.2 but with large fluctuations (Heiles 2001a). It strikes us that the amount, thermal state, and ionization state of the WNM are sensitive indicators of the conflicting effects of dynamical (macrophysical) and atomic (microphysical) processes, both of which heat and cool the gas. In addition, microphysical processes heat by ionizing the gas, while macrophysical ones usually do not.

12.1. Microphysical processes

Microphysical processes include the ones treated by WHMT, which rely on well-known radiation energy densities. However, these are not necessarily so well-known as we would wish. Consider, for example, the production of the Warm Ionized Medium (WIM) by ionizing photons. Classically, we expect ionizing photons to be strictly limited to their Strömgren spheres; in fact, however, the photons can diffuse out to large distances and produce the WIM, which produces pulsar dispersion and diffuse Hα emission. The diffusion efficiency is only partially understood (Miller & Cox 1993; Dove & Shull 1993). This shows that we do not completely understand photon propagation in the ISM.

We wish to mention two additional microphysical processes that might be underappreciated and add significant heating. Both of these act preferentially on low-density gas and thus affect the WNM more than the CNM. The first process is low-energy cosmic rays, whose energy density cannot be measured directly because they are excluded from the Solar System. Geballe et al (1999) observe H_3^+ to be much more abundant than predicted in diffuse clouds; a probable reason is a considerable excess of low-energy cosmic rays over the current standard value. Such cosmic rays ionize and heat the ISM.

The second is X-rays from soft gamma-ray repeaters. Consider the specific example of the famous 27 Aug 1998 event of SGR 1900+14, which was the most powerful of many bursts produced by an object $\sim$ 6 kpc distant (see Feroci et al 2001 for a review). This particular burst produced enough X rays to ionize the nighttime Earth's atmosphere to the extent normally found in daytime. This, in turn, required X rays whose energies are so large that they are of little interest for ISM heating (because the interaction cross sections are small). However, it strikes us as unlikely that the intrinsic X-ray spectrum cuts off at low energies. Rather, the lower-energy X rays are easily absorbed by the ISM. Bursts from the ensemble of gamma-ray repeaters in a galaxy might be a significant energy source for heating the WNM. If so, the limited lifetime of soft gamma ray repeaters would probably produce conditions mimicking time-dependent models of the ISM such as that of Gerola, Kafatos, & McCray (1974).

12.2. Macrophysical processes

There exist several dynamical processes that can heat the ISM. These, like the microphysical ones mentioned above, preferentially heat the WNM over the CNM. These processes include hydromagnetic wave heating (Ferriere, Zweibel, & Shull 1988), MHD turbulence (Mintner & Spangler 1997), magnetic reconnection (Vishniac & Lazarian 1999), scattered shocks (acoustic waves or "thunder"; Ikeuchi & Spitzer 1984), turbulence (e.g. Gazol et al 2001), and turbulent mixing layers at the boundaries of neutral clouds (Slavin, Shull, & Begelman 1993). When we think of shocks we usually think of supernovae. However, shocks are produced by other methods on both small and large scales. Examples at small scales include ejecta from newly forming stars, HII regions, and cloud collisions. At large scales we have Galactic dynamics and gravitation of large clouds (Wada & Norman 1999, 2001; Walters & Cox 2001).

Some of the above-quoted references calculate distribution functions of gas temperature and density. They find thermally unstable gas and conclude that macroscopic dynamical processes overshadow the microscopic ones in determining gas temperature. These macrophysical processes are hard to calculate because they depend indirectly on coupling to many forms of energy input.

12.3. Commentary

The WNM is the key to the Universe because the amount, temperature, and ionization state of the WNM depend on many processes. Most of the processes we have mentioned depend on energy sources that cannot be characterized without a *global* understanding of *many* different types of objects, and most of these we know very little about. When global ISM models are successful in predicting the observed WNM properties, including the amount, thermal state, and ionization state, then we will have made a significant step forward in understanding many aspects of not only the interstellar medium but also all of its associated energy sources. These include many objects of general interest in the Galaxy such as, for example, the Galactic dynamo, spiral density wave shocks, supernovae, and soft gamma-ray repeaters.

We thank Leo Blitz, Tom Dame, James Graham, Dave Hollenbach, Ed Jenkins, Chris McKee, Mike Shull, Phil Solomon, Patricia Vader, and Mark Wolfire for helpful discussions. CH is indebted to the UC Berkeley Astronomy Department for providing the freedom and time to construct and teach a course in numerical data analysis, from which experience some of the current data analysis greatly benefited. This work was supported in part by NSF grants AST-9530590, AST-0097417, AST-9988341, and by the NAIC.

REFERENCES

Arce, H.G. & Goodman, A.A. 1999, ApJ, 517, 264.

Binney, J. & Merrifield, M. 1998, Galactic Astronomy, (Princeton University Press: Princeton), p 137.

Boulares, A. & Cox, D.P. 1990, ApJ, 365, 544.

Crovisier, J. 1981, A&A, 94, 162.

Crovisier, J., Kazès, I., and Aubry, D. 1978, A&AS, 32, 205.

Dame, T.M. et al 1987, ApJ, 322, 706.

Dame, T.M., Hartmann, D., & Thaddeus, P. 2001, ApJ, 547, 792.

Dickey, J.M. 1979, ApJ, 233, 558.

Dickey, J.M., Salpeter, E.E., & Terzian, Y. 1978, ApJS, 36, 77 (DST).

Dickey, J.M., Mebold, U., Stanimirovic, S., & Staveley-Smith, L. 2000, ApJ, 536, 756.

Dove, J.B. & Shull, J.M. 1994, ApJ, 430, 222.

Dunteman, G.H. 1984, Introduction to Multivariate Analysis, Sage Publications (Beverly Hills), p. 156-180.

Egger, R. 1998, in The Local Bubble and Beyond, ed. D. Breitschwerdt, M.J. Freyberg, & J. Trümper, (Springer:Berlin), p 287.

Feroci, M., Hurley, K., Duncan, .R.C., & Thompson, C. 2001, ApJ, 549, 1021.

Ferriere, K.M., Zweibel, E.G., & Shull, J.M. 1988, ApJ, 332, 984.

Gazol, A., Vázquez-Semadeni, E., Sánchez-Salcdeo, F.J., & Scalo, J. 2001, ApJ, 557, L121.

Geballe, T.R., McCall, B.J., Hinkle, K.H., & Oka, T. 1999, ApJ, 510, 251.

Gerola, H., Kafatos, M., & McCray, R. 1974, ApJ, 189, 55.

Haffner, L.M., Reynolds, R.J., & Tufte, S.L. 1998, ApJ, 501, L83.

Hartmann, D., & Burton, W.B. 1997, Atlas of Galactic Neutral Hydrogen, Cambridge U. Press.

Heiles, C. 1967, ApJS, 15, 97.

Heiles, C. 1998, ApJ, 498, 689.

Heiles, C. 2001a, in Tetons 4: Galactic Structure, .Stars, and the Interstellar Medium, ed. C.E. Woodward, M.D. Bicay, & J.M. Shull, ASP Conf Series 231.

Heiles, C. 2001b, ApJ, 551, L108.

Heiles, C. 2002, *http://astron.berkeley.edu/~heiles/ay250/lsfit_2002.ps* .

Heiles, C. & Troland, T. 2002, apj, 000, 000 (Paper I).

Hester, J.J. 1987, ApJ, 314, 187.

Gibson, S.J., Taylor, A.R., Higgs, L.A., & Dewdney, P.E. 2000, ApJ, 540, 851.

Gibson, S.J. 2001, in Seeing Through the Dust, ed. R. Taylor, T. Landecker, T. Willis, ASP Conf Series 000.

Greisen, E.W. and Liszt, H.S. 1986, ApJ, 303, 702.

Ikeuchi, S. & Spitzer, L. 1984, ApJ, 283, 825.

Jenkins, E.B. & Tripp, T.M. 2001, ApJS, 137, 297.

Lazereff, B. 1975, A&A, 42, 25.

Lebart, L., Morineau, A., & Warwick, K.M. 1984, Multivariate Descriptive Statistical Analysis, John Wiley & Sons (New York),m p. 1-29.

Liszt, H.S. 1983, ApJ, 275,, 163.

Liszt, H.S. 2001, ApJ, 371, 698.

Kalberla, P.M.W., Schwarz, U.J. & Goss, W.M. 1985, A&A, 144, 27.

Knapp, G.R. & Verschuur, G.L. 1972, AJ, 17, 717.

Kulkarni, S.R. & Heiles, C. 1987, in Interstellar Processes, ed. D.J. Hollenbach & H.A. Thronson, Jr., (Reidel:Dordrecht), p 87.

Ladd, E.F., Myers, P.C.m & Goodman, A.A. 1994, ApJ, 433, 117.

Marx-Zimmer, M., Herbstmeier, U., Zimmer, F., Dickey, J.M., Staveley-Smith, L., & Mebold, U. 2000, A&A, 354, 787.

McKee, C.F. 1993, in Back to the Galaxy, ed. S.S. Holt & F. Verter, (AIP Press, New York), p 499

McKee, C.F. & Ostriker, J.P. 1977, ApJ, 218, 148.

Mebold, U., Düsterberg, C., Dickey, J.M., Staveley-Smith, L., & Kalberla, P. 1997, ApJ, 490, L65.

Mebold, U., Winnverb, A., Kalberla, P.M.W., & Goss, W.M. 1982, A&A, 115, 223.

Miller, W.W. & Cox, D.P. 1993, ApJ, 417, 579.

Mintner, A.H. & Spangler, S.R. 1997, ApJ, 485, 182.

Murtagh, F. & Heck, A. 1987, Reidel (Dordrecht), p 13-54.

Payne, H.E., Salpeter, E.E., & Terzian, Y. 1983, ApJ, 272, 540 (PST).

Rohlfs, K. & Wilson, T.L. 2000, Tools of Radio Astronomy, Springer.

Savage, B.D., Drake, J.F., Budich, W., & Bohlin, R.C. 1977, ApJ, 216, 291

Sfeir, D.M., Lallement, R., Crifo, F., & Welsh, B.Y. 1999, A&A, 346, 785.

Shull, M.J. et al 2000, ApJ, 538, L73.

Slavin, J.D., Shull, J.M., & Begelman, M.C. 1993, ApJ, 407, 83.

Stetson, P.B. 2002, *http://nedwww.ipac.caltech.edu/level5/Stetson/Stetson4.html.*

Vishniac, E.T. & Lazarian, A. 1999, ApJ, 511, 193.

Wada, K. & Norman, C.A. 1999, ApJ, 516, L13.

Wada, K. & Norman, C.A. 2001, ApJ, 547, 172.

Walters, M.A. & Cox, D.P. 2001, ApJ, 549, 353.

Wolfire, M.G., Hollenbach, D., McKee, C.F., Tielens, A.G.G.M., & Blakes, E.L.O. 1995, ApJ, 443, 152 (WHMT).

Wolfire, M.G., McKee, C.F., Hollenbach, D., Tielens, A.G.G.M. 2002, ApJ, submitted.

Table 1. Source list

Source	RA_{1950}	DEC_{1950}	l	b	FLUX (Jy)	$N(HI)_{WNM}$	$N(HI)_{CNM}$	$N(HI)_{tot}$
3C18	00 38 14	09 46 55	118.62	-52.73	5.02 ± 0.07	0.75	5.23	5.98
3C33-1	01 06 12	13 02 31	129.44	-49.34	8.70 ± 0.00	0.86	1.95	2.80
3C33	01 06 14	13 03 36	129.45	-49.32	8.84 ± 0.14	1.14	1.64	2.78
3C33-2	01 06 17	13 06 21	129.46	-49.28	3.75 ± 0.00	1.02	1.90	2.92
3C64	02 19 19	08 13 18	157.77	-48.20	1.78 ± 0.00	3.42	2.91	6.34
3C75-1	02 55 00	05 51 49	170.22	-44.91	2.83 ± 0.00	5.92	2.05	7.97
3C75	02 55 05	05 50 43	170.26	-44.91	3.93 ± 0.04	5.40	2.48	7.88
3C75-2	02 55 09	05 49 14	170.30	-44.92	2.44 ± 0.00	6.09	2.14	8.22
3C78	03 05 49	03 55 13	174.86	-44.51	7.22 ± 0.07	4.25	5.82	10.07
3C79	03 07 11	16 54 35	164.15	-34.46	4.25 ± 0.00	2.46	6.91	9.36
CTA21	03 16 09	16 17 39	166.64	-33.60	8.22 ± 0.00	6.43	3.13	9.56
P0320+05	03 20 41	05 23 33	176.98	-40.84	2.67 ± 0.00	6.15	5.04	11.19
NRAO140	03 33 22	32 08 36	159.00	-18.76	2.62 ± 0.00	16.06	13.42	29.49
3C93.1	03 45 35	33 44 05	160.04	-15.91	2.10 ± 0.00	8.83	3.50	12.33
P0347+05	03 47 07	05 42 33	182.27	-35.73	3.06 ± 0.00	6.18	7.26	13.44
3C98-1	03 56 07	10 15 22	179.86	-31.09	4.00 ± 0.11	4.38	5.99	10.37
3C98	03 56 11	10 17 40	179.84	-31.05	6.18 ± 0.00	4.92	6.10	11.02
3C98-2	03 56 14	10 18 59	179.83	-31.02	6.21 ± 0.00	5.19	5.05	10.25
3C105	04 04 44	03 33 25	187.63	-33.61	3.74 ± 0.32	3.26	11.42	14.68
3C109	04 10 55	11 04 35	181.83	-27.78	3.46 ± 0.08	5.31	15.52	20.82
P0428+20	04 28 06	20 31 11	176.81	-18.56	3.66 ± 0.00	17.00	6.90	23.90
3C120	04 30 31	05 14 58	190.37	-27.40	5.71 ± 0.03	8.04	7.90	15.93
3C123	04 33 55	29 34 13	170.58	-11.66	53.55 ± 2.11	19.75	7.62	27.37
3C131	04 50 10	31 24 31	171.44	-7.80	2.99 ± 0.13	17.27	11.28	28.55
3C132	04 53 42	22 44 41	178.86	-12.52	3.83 ± 0.03	16.16	7.66	23.81
3C133	04 59 54	25 12 11	177.73	-9.91	5.93 ± 0.04	19.15	9.35	28.50
3C138	05 18 16	16 35 25	187.41	-11.34	7.31 ± 0.12	9.16	10.70	19.85
3C141.0	05 23 27	32 47 35	174.53	-1.31	2.01 ± 0.04	29.05	23.64	52.69
T0526+24	05 26 05	24 58 30	181.36	-5.19	1.13 ± 0.00	26.33	70.53	96.86
3C142.1	05 28 48	06 28 16	197.62	-14.51	3.13 ± 0.00	13.85	8.11	21.96
P0531+19	05 31 47	19 25 17	186.76	-7.11	6.90 ± 0.12	14.30	9.54	23.84
T0556+19	05 56 58	19 08 45	190.09	-2.17	0.97 ± 0.00	53.63	0.00	53.63
4C22.12	06 00 50	22 00 54	188.05	0.05	2.16 ± 0.05	31.58	53.65	85.23
3C154	06 10 42	26 05 27	185.59	4.00	5.39 ± 0.02	26.72	8.84	35.57
T0629+10	06 29 29	10 24 16	201.53	0.51	2.60 ± 0.05	22.23	37.02	59.25
3C167	06 42 36	05 34 48	207.31	1.15	1.72 ± 0.01	19.39	30.85	50.24
3C172.0	06 59 04	25 18 06	191.20	13.41	2.56 ± 0.00	7.31	0.40	7.71
DW0742+10	07 42 48	10 18 33	209.80	16.59	3.47 ± 0.00	2.43	0.00	2.43
3C190.0	07 58 45	14 23 02	207.62	21.84	2.41 ± 0.00	2.82	0.00	2.82
3C192	08 02 35	24 18 34	197.91	26.41	4.41 ± 0.02	3.50	0.47	3.97
P0820+22	08 20 28	22 32 46	201.36	29.68	2.17 ± 0.00	4.23	0.00	4.23
3C207	08 38 01	13 23 06	212.97	30.14	2.48 ± 0.05	4.34	0.91	5.24

Table 1—Continued

Source	RA_{1950}	DEC_{1950}	l	b	FLUX (Jy)	$N(HI)_{WNM}$	$N(HI)_{CNM}$	$N(HI)_{tot}$
3C208.0	08 50 23	14 04 16	213.66	33.16	2.51 ± 0.03	2.99	0.00	2.99
3C208.1	08 51 54	14 17 16	213.60	33.58	2.24 ± 0.03	2.76	0.00	2.76
3C223	09 36 50	36 07 41	188.40	48.66	1.47 ± 0.00	0.98	0.00	0.98
3C225a	09 39 25	14 05 36	219.87	44.02	1.34 ± 0.01	1.89	1.51	3.40
3C225b	09 39 32	13 59 30	220.01	44.01	3.78 ± 0.03	2.42	0.86	3.28
3C228.0	09 47 27	14 34 00	220.40	45.99	3.48 ± 0.07	2.24	0.37	2.61
3C234	09 58 56	29 01 40	200.21	52.70	4.64 ± 0.00	1.61	0.00	1.61
3C236	10 03 05	35 08 49	190.06	53.98	2.66 ± 0.00	1.20	0.00	1.20
3C237	10 05 22	07 44 58	232.12	46.63	7.66 ± 0.07	0.65	1.55	2.20
3C245	10 40 06	12 19 15	233.12	56.30	3.12 ± 0.08	1.55	0.48	2.04
P1055+20	10 55 37	20 08 02	222.51	63.13	2.64 ± 0.29	1.20	0.36	1.56
P1117+14	11 17 51	14 37 22	239.45	65.26	2.39 ± 0.00	1.57	0.00	1.57
3C263.1	11 40 49	22 23 37	227.20	73.77	3.14 ± 0.00	1.69	0.00	1.69
3C264.0	11 42 32	19 53 56	235.70	73.05	4.22 ± 0.00	1.73	0.00	1.73
3C267.0	11 47 22	13 04 00	254.81	69.68	2.27 ± 0.00	2.32	0.00	2.32
3C272.1	12 22 32	13 09 40	278.21	74.48	5.57 ± 0.00	2.04	0.36	2.40
3C273	12 26 32	02 19 39	289.95	64.36	56.13 ± 1.12	1.43	0.50	1.93
3C274.1	12 32 57	21 37 06	269.87	83.16	2.19 ± 0.02	2.06	0.30	2.35
4C07.32	13 13 46	07 18 18	320.42	69.07	1.55 ± 0.00	1.79	0.32	2.11
4C32.44	13 23 58	32 09 53	67.24	81.04	4.47 ± 0.05	0.91	0.14	1.05
3C286	13 28 49	30 46 02	56.53	80.67	18.36 ± 0.00	2.05	0.00	2.05
3C293	13 50 02	31 41 43	54.61	76.06	4.50 ± 0.00	1.29	0.00	1.29
4C19.44	13 54 42	19 33 44	8.99	73.04	2.52 ± 0.11	2.66	0.00	2.66
4C20.33	14 22 37	20 14 01	19.54	67.46	1.89 ± 0.01	2.15	0.53	2.68
3C310	15 02 48	26 12 36	38.50	60.21	5.12 ± 0.04	2.60	1.11	3.71
3C315	15 11 31	26 18 37	39.36	58.30	4.49 ± 0.03	2.54	2.22	4.76
3C318	15 17 50	20 26 54	29.64	55.42	2.90 ± 0.02	3.01	1.74	4.75
3C333	16 15 05	21 14 51	37.30	42.97	1.89 ± 0.01	3.99	1.10	5.09
3C348	16 48 40	05 04 28	23.05	28.95	46.11 ± 0.75	4.15	1.55	5.70
3C353	17 17 54	00-55 55	21.20	19.64	48.76 ± 1.70	3.84	7.00	10.85
4C13.65	17 56 13	13 28 42	39.31	17.72	2.40 ± 0.06	7.72	1.46	9.18
4C13.67	18 35 12	13 28 03	43.50	9.15	1.69 ± 0.01	12.76	3.96	16.72
3C409	20 12 18	23 25 42	63.40	-6.12	17.08 ± 0.15	19.73	6.06	25.79
3C410	20 18 03	29 32 35	69.21	-3.77	10.06 ± 0.00	32.78	15.44	48.22
3C433	21 21 30	24 51 17	74.48	-17.69	13.22 ± 0.15	5.06	2.83	7.89
3C454.0	22 49 07	18 32 44	87.35	-35.65	2.29 ± 0.03	4.13	1.24	5.37
3C454.3	22 51 29	15 52 56	86.11	-38.18	17.22 ± 0.38	4.80	1.72	6.53

Note. — Flux is in Jy and includes the contribution from all extended components; HI column densities are in units of 10^{20} cm^{-3}.

Note. — Some sources having $|b| < 10^\circ$ have very complicated HI profiles and have unacceptable, unreliable fits. Their results should not be used. These sources include T0526+24, T0556+19, 4C22.12, T0629+10, 3C167.

Table 2. Medians and Means of CNM T_s

b-range	Median T_s	Mean T_s
CNM, $\|b\| > 10°$, by N_G	48	88
CNM, $\|b\| > 10°$, by $N_(HI)$	70	108
CNM, $\|b\| < 10°$, by N_G	47	71
CNM, $\|b\| < 10°$, by $N_(HI)$	63	99

Note. — Temperatures are in Kelvins. "by N_G" means that the median and mean are taken over Gaussian components with no weighting by $N(HI)$. "by $N(HI)$" means that half the column density lies above, and half below, the median; and the mean is weighted by $N(HI)$.

Note. — Figure 2 presents the histograms, which have long tails at high T_s so that neither the median nor the mean represent the typical values.

Table 3. Medians and Means of $N(HI)$

b-range	Median $N(HI)_{20}$	Mean $N(HI)_{20}$
CNM, $\|b\| > 10°$	0.52	1.27
CNM, $\|b\| < 10°$	1.97	5.00
WNM, $\|b\| > 10°$	1.30	2.04
WNM, $\|b\| < 10°$	8.13	12.03

Note. — $N(HI)_{20}$ is HI column density in units of 10^{20} cm^{-2}. Figure 4 presents the histograms.

Table 4. Spin versus H_2 Temperatures for proximate positions

Source	(l, b)	$N(HI)$	T
NEAR $(l, b) = (160°, -17°)$:			
NRAO140	$(159.0, -18.8)$	13.4	27 ± 13
3C93.1	$(160.0, -15.9)$	1.8	29 ± 11
HD21856	$(156, -17)$	11.0	84
HD22951	$159, -17)$	11.0	63
HD23180	$(160, -18)$	7.9	48
NEAR $(l, b) = (196°, -13°)$:			
HD24398	$(162, -17)$	6.5	57
3C142.1	$(197.6, -14.5)$	7.0	49 ± 16
HD36822	$(195, -13)$	6.5	63
NEAR $(l, b) = (234°, 55°)$:			
HD36861	$(195, -12$	6.0	45
3C245	$(233.1, 56.3)$	0.5	510 ± 8
HD91316	$(235, 53)$	1.8	377

Note. — For radio source results, only the CNM component with the largest $N(HI)$ is listed. $N(HI)$ is in units of 10^{20}. Stars are from Savage et al (1977).

Table 5. CNM fluctuations for closely-spaced sources

Sources	(l, b)	$\Delta\theta$	T_{exp}	τ_0	$VLSR$	$FWHM$	T_s	$N(HI)$	AREA
$\frac{\mathrm{3C225a}}{\mathrm{3C225b}}$	$(220.0, 44.0)$	6.3	$\frac{5.8}{9.2}, 1.6$	$\frac{0.31}{0.75}, 2.5$	$\frac{4.0}{3.6}, 0.30$	$\frac{1.3}{1.3}, 1.0$	$\frac{22}{17}, 1.2$	$\frac{0.17}{0.32}, 1.9$	$\frac{0.32}{0.73}, 2.3$
$\frac{\mathrm{3C33-1}}{\mathrm{3C33-2}}$	$(129.4, -49.3)$	4.2	$\frac{10.4}{10.2}, 1.0$	$\frac{0.034}{0.059}, 1.7$	$\frac{-4.6}{-4.2}, 0.02$	$\frac{9.4}{9.3}, 1.0$	$\frac{310}{178}, 1.7$	$\frac{2.0}{1.9}, 1.0$	$\frac{0.25}{0.43}, 1.7$
$\frac{\mathrm{3C75-1}}{\mathrm{3C75-2}}$	$(170.3, -44.9)$	3.4	$\frac{18}{17}, 1.1$	$\frac{0.73}{0.65}, 1.1$	$\frac{-10.4}{-10.4}, 0.0$	$\frac{2.1}{2.3}, 1.1$	$\frac{35}{36}, 1.0$	$\frac{1.0}{1.1}, 1.1$	$\frac{1.2}{1.2}, 1.0$
$\frac{\mathrm{3C75-1}}{\mathrm{3C75-2}}$	$(170.3, -44.9)$	3.4	$\frac{1.3}{3.1}, 2.3$	$\frac{0.082}{0.094}, 1.1$	$\frac{-6.1}{-6.0}, 0.04$	$\frac{3.0}{2.3}, 1.3$	$\frac{17}{34}, 2.1$	$\frac{0.08}{0.15}, 1.9$	$\frac{0.19}{0.18}, 1.0$
$\frac{\mathrm{3C75-1}}{\mathrm{3C75-2}}$	$(170.3, -44.9)$	3.4	$\frac{10}{10}, 1.0$	$\frac{0.13}{0.13}, 1.1$	$\frac{5.0}{4.9}, 0.02$	$\frac{4.6}{4.4}, 1.0$	$\frac{84}{78}, 1.1$	$\frac{0.95}{0.93}, 1.0$	$\frac{0.45}{0.48}, 1.1$
$\frac{\mathrm{3C98-1}}{\mathrm{3C98-2}}$	$(179.8, -31.0)$	4.0	$\frac{1.7}{5.1}, 3.1$	$\frac{0.081}{0.090}, 1.1$	$\frac{-1.2}{-1.5}, 0.09$	$\frac{3.2}{3.2}, 1.0$	$\frac{21}{59}, 2.8$	$\frac{0.11}{0.33}, 3.0$	$\frac{0.21}{0.22}, 1.0$
$\frac{\mathrm{3C98-1}}{\mathrm{3C98-2}}$	$(179.8, -31.0)$	4.0	$\frac{7.8}{4.5}, 1.7$	$\frac{0.21}{0.20}, 1.0$	$\frac{9.4}{9.5}, 0.07$	$\frac{1.5}{1.4}, 1.1$	$\frac{41}{24}, 2.8$	$\frac{0.25}{0.13}, 1.9$	$\frac{0.24}{0.21}, 1.1$
$\frac{\mathrm{3C98-1}}{\mathrm{3C98-2}}$	$(179.8, -31.0)$	4.0	$\frac{35}{36}, 1.0$	$\frac{0.37}{0.45}, 1.2$	$\frac{9.7}{9.6}, 0.07$	$\frac{6.1}{4.6}, 1.3$	$\frac{115}{100}, 1.2$	$\frac{5.0}{4.1}, 1.2$	$\frac{1.4}{1.6}, 1.1$
$\frac{\mathrm{3C98-1}}{\mathrm{3C98-2}}$	$(179.8, -31.0)$	4.0	$\frac{5.9}{5.7}, 1.0$	$\frac{0.028}{0.035}, 1.3$	$\frac{22.8}{22.5}, 0.06$	$\frac{5.4}{4.6}, 1.2$	$\frac{216}{166}, 1.3$	$\frac{0.63}{0.52}, 1.2$	$\frac{0.63}{0.52}, 1.2$
$\frac{\mathrm{3C310}}{\mathrm{3C315}}$	$(38.9, 59.4)$	118	$\frac{18}{24}, 1.3$	$\frac{0.62}{0.78}, 1.3$	$\frac{-3.7}{-4.2}, 0.25$	$\frac{1.8}{2.2}, 1.2$	$\frac{39}{44}, 1.1$	$\frac{0.82}{1.5}, 1.8$	$\frac{0.85}{1.3}, 1.5$
$\frac{\mathrm{3C310}}{\mathrm{3C315}}$	$(38.9, 59.4)$	118	$\frac{2.9}{8.3}, 2.9$	$\frac{0.061}{0.15}, 2.4$	$\frac{0.6}{1.6}, 0.21$	$\frac{5.1}{4.4}, 1.2$	$\frac{49}{61}, 1.3$	$\frac{0.29}{0.77}, 2.7$	$\frac{0.24}{0.50}, 2.0$

Note. — Parameters for closely-spaced source pairs are listed as fractions, with the numerators and denominators corresponding to the appropriate component. Immediately to the right of each fraction we write the ratio, which is always expressed as being > 1 for purposes of comparison among sources. For $VLSR$, however, instead of writing the ratio we write the velocity difference divided by the linewidth $FWHM$. $\Delta\theta$ is the angular separation in arcmin, T_{exp} the central brightness of the component in the expected profile, $VLSR$ the LSR velocity, $FWHM$ the line halfwidth, T_s the spin temperature, τ the central opacity, $N(HI)$ the HI column density in units of 10^{20} cm^{-2}, and AREA is 0.72 times the line area in km s^{-1} (which is equal to $N(HI)_{20}$ if $T_s = 40$ K).

Table 6. GL's fluctuation statistics for two components in 3C348

V_{LSR}	τ_0	T_s	$N(HI)_{CNM}$	$\frac{\sigma(N(HI)}{N(HI)}$
0.5	0.604 ± 0.004	32.5 ± 5.8	0.81	0.25
–2.2	0.259 ± 0.003	11.6 ± 4.8	0.10	0.10

Note. — The first four columns are our Gaussian component data. The fifth column is GL's rms profile area divided by the mean profile area for the 5 positions listed in their Table 4.